Fragmentation Cross Sections of Medium-Energy ^{35}Cl, ^{40}Ar, and ^{48}Ti Beams on Elemental Targets

C. Zeitlin,* S. Guetersloh, L. Heilbronn, and J. Miller
Lawrence Berkeley National Laboratory, Berkeley, CA 94720

A. Fukumura, Y. Iwata, and T. Murakami
National Institute of Radiological Sciences, Chiba, Japan

L. Sihver and D. Mancusi
Chalmers University of Technology, SE-412 96 Göteborg, Sweden
(Dated: December 11, 2007)

Charge-changing and fragment production cross sections at 0° have been obtained for interactions of 290, 400, and 650 MeV/nucleon ^{40}Ar beams, 650 and 1000 MeV/nucleon ^{35}Cl beams, and a 1000 MeV/nucleon ^{48}Ti beam. Targets of C, CH_2, Al, Cu, Sn, and Pb were used. Using standard analysis methods, we obtain fragment cross sections for charges as low as 8 for Cl and Ar beams, and as low as 10 for the Ti beam. Using data obtained with small-acceptance detectors, we report fragment production cross sections for charges as low as 5, corrected for acceptance using a simple model of fragment angular distributions. With the lower-charged fragment cross sections, we can compare the data to predictions from several models (including NUCFRG2, EPAX2, and PHITS) in a region largely unexplored in earlier work. As found in earlier work with other beams, NUCFRG2 and PHITS predictions agree reasonably well with the data for charge-changing cross sections, but do not accurately predict the fragment production cross sections. The cross sections for the lightest fragments demonstrate the inadequacy of several models in which the cross sections fall monotonically with the charge of the fragment. PHITS, despite not agreeing particularly well with the fragment production cross sections on average, nonetheless qualitatively reproduces some significant features of the data that are missing from the other models.

PACS numbers: 25.75.-q, 25.70.Mn, 25.60.Dz, 24.10.Lx, 98.70.Sa

I. INTRODUCTION

Heavy ions in the Galactic Cosmic Rays (GCR) contribute substantially to the dose and dose equivalent received in spaceflight [1]. This will be especially significant when future missions take astronauts outside the shielding of the geomagnetosphere for long periods of time. Due to limited knowledge of the relevant cross sections, calculations of dose – which necessarily involve fragmentation of energetic heavy ions in spacecraft walls, astronauts' bodies, habitat shielding, etc. – can be highly uncertain [2]. Radiation protection requirements force planners to err on the side of caution, and as a consequence, large uncertainties in fragmentation cross sections may be a factor in limiting mission duration, and/or impose large costs to adequately shield inhabited areas. An accurate and precise database of the nuclear interaction cross sections is an essential tool for the development of transport models with reduced uncertainty compared to current models. In the following, we refer to two types of cross sections: charge-changing (sometimes referred to as "total" charge-changing) and fragment production. The latter are partial cross sections, and – given the detection and analysis methods used here – the sum over all fragment species is, in each case, equal to the charge-changing cross section. (This statement pertains to the fragment cross sections uncorrected for acceptance.)

The charge-changing cross sections reported here, using ions close to one another in charge and mass, show some deviations from the predictions of purely geometric models, and also exhibit mild energy dependence for hydrogen targets, as seen in previous experiments. Fragment production cross sections reported here and in previous work also show subtle energy dependences, for all targets, not just H. These behaviors highlight the inadequacy of energy-independent models and present valuable tests of the accuracy of more sophisticated models, which in spite of much effort on the development side, still fail to replicate important features of the data. The measurements reported here were made using 290, 400, and 650 MeV/nucleon ^{40}Ar beams, 650 and 1000 MeV/nucleon ^{35}Cl beams, and a 1000 MeV/nucleon ^{48}Ti beam. Targets of C, CH_2, Al, Cu, Sn, and Pb were used. These measurements are part of an ongoing series of experiments intended to spur the development and refinement of space radiation transport models.

An additional test of the models is provided by our ability to extract fragment cross sections for charges as low as 5, using the spectra obtained with detectors placed relatively far from the target, so as to subtend small acceptance angles (the half-angle of the forward cone defined by the center of the target and the edge of a given

*Electronic address: cjzeitlin@lbl.gov

detector). Fragment cross sections obtained with these detectors are corrected for acceptance using a model based on Goldhaber's formulation of angular distributions [3], which has been shown to work well for other data sets [4, 5]. Due to uncertainties in the σ_0 parameter that determines the momentum widths in the model, the acceptance correction is a source of additional uncertainty, as explained in detail below. We also compare the results obtained here to those obtained in other experiments [6–8]. Comparisons of the fragmentation cross sections from ^{36}Ar and ^{40}Ar beams are of particular interest, as the observed differences in the fragment cross sections have been ascribed to the differing isospin values ($T_z = 0$ and T_z = -2, respectively) of the beam ions. This is potentially an important effect to understand for purposes of modeling or parameterizing the systematics of fragmentation. In the present work, though we do not have data for ^{36}Ar, the ^{35}Cl data are available for comparison of different isospins, as it has $T_z = -1/2$ while the two other beam ions both have $T_z = -2$. When examining the odd-even effect in these data, we also consider other recently-published data of ours, using beams of ^{28}Si, and older data from Chen et al. [9] for ^{40}Ca, to provide comparisons with $T_z = 0$ projectiles.

The Webber et al. and Knott et al. experiments mentioned above focused on hydrogen targets, for the purpose of understanding the propagation of GCR through the interstellar medium. More recent work by Webber et al. [10] provides a wealth of data and predictions for hydrogen-target cross sections. The Iancu et al. work [8], though using CR-39 instead of active detectors, is in many ways more similar to the study presented here in terms of the choice of targets, which span the periodic chart and allow us to study the dependence of the cross sections on target mass. This type of systematic study is more appropriate for the general issue of radiation protection in deep space, since we cannot yet say which materials will be used in the construction of space vehicles and other habitats.

II. EXPERIMENTAL CONFIGURATIONS

We report here several separate but similarly designed experiments. Those with ^{40}Ar beams were performed at the Heavy Ion Medical Accelerator in Chiba (HIMAC) at the Japanese National Institute of Radiological Sciences, using beams at extracted energies of 290, 400, and 650 MeV/nucleon. The 650 and 1000 MeV/nucleon ^{35}Cl and 1000 MeV/nucleon ^{48}Ti beam data were obtained at the NASA Space Radiation Laboratory (NSRL) at the Brookhaven National Laboratory. The experiments, like several others previously reported by our group [4, 5, 11–15], are designed to identify particles using deposited energy (ΔE) use signals from small-area silicon detectors placed directly on the beam axis. Detectors are positioned just upstream of the target position so that a clean sample of events (with one and only one well-identified primary beam ion, close to the beam axis) can be selected in the off-line analysis. Additional detectors are placed at various distances with respect to the target-center position so that they subtend different acceptance angles. Spectra obtained with large acceptance detectors, typically with active radii of about 2 cm placed within about 10 cm of the target exit, have 100% acceptance for surviving primaries and all fragments whose species can be identified, which generally extends as far as charges $Z_{frag} \geq Z_{primary}/2$. Below about $Z_{primary}/2$, there is no resolution of species since the many possible combinations of light fragments produce overlapping ΔE distributions. Detectors placed downstream so as to have small acceptance, on the order of 1° to 2°, are hit by a much smaller multiplicity of fragments, and produce spectra in which there is typically resolution of all fragment species. However, due to many ambiguities in interpretation of the peaks for the lightest fragments (and combinations of fragments), we confine the present analysis to charges 5 and higher. This point will be discussed further below.

The data obtained with 290 MeV/nucleon ^{40}Ar do not allow for analysis of light fragments below charge 10, though the experimental configuration was quite similar to the others reported here. Several factors combine to make the data from the downstream detectors unusable for cross section analysis for this beam. First, owing to the low energy and high dE/dx of the primary beam ions, targets were kept quite thin, yielding poor fragment statistics. Second, even with thin targets, there is significant energy loss in the targets and detectors, enough to make the fragment velocity distributions quite broad and to cause the ΔE peaks from neighboring species to overlap one another considerably. This effect worsens as depth in the stack increases, and thus the light-fragment peaks in the small acceptance detectors are generally not well defined. Finally, the low beam energy causes the fragment angular distributions to be less forward-peaked than in the other data sets reported here, so that many light fragments are outside the acceptances of the small-angle detectors, further depleting the already poor statistics. For these reasons, we are able only to report the fragment cross sections in the large-acceptance detector pair, where charges as low as 10 can be resolved.

Figure 1 is a schematic drawing of the arrangement of detectors on the beamline for the ^{35}Cl experiments; Figure 2 shows the arrangement for the 400 MeV/nucleon ^{40}Ar experiment; and Figure 3 shows the arrangement for the ^{48}Ti experiment. Table 1 enumerates the types of detectors and their acceptance angles. The detectors downstream of the target position are of three types: 3 mm depth with 1.1 cm active radius, referred to as 3mmN where N is the number of a particular detector of this type, in order of increasing distance from the target; 5 mm depth with 1.9 cm active radius, referred to as 5mmN; and 0.85 to 1 mm depth position-sensitive detectors (PSDs) with 2.0 cm active radius, referred to as PSDN where N refers to an x-y detector pair. All three types are lithium-drifted. They are typically arranged

in pairs to facilitate the data analysis, which depends on correlation cuts (described below) in neighboring detectors. The PSDs also provide position information for the x and y coordinates (in the plane orthogonal to the beam direction). The position data are not used in the present analysis, although potentially some information about fragment angular distributions could be extracted from them.

Although the set of target materials was the same across experiments, the depths were varied. The target depths, in units of interaction lengths (as calculated by the energy-independent geometric model of Wilson et al. [16]), were between 2.7% and 43%. Those are the extreme cases; typically, targets presented 5% to 15% of an interaction length to the primary beam ions. In general, for the lower beam energies used here, targets must be kept thin to avoid excessive energy loss; for the higher beam energies, increased depths can be used, giving a more precise measurement of the charge-changing cross sections, but necessitating relatively large corrections for secondary and higher-order interactions that alter the distributions of fragments exiting the target. Unlike earlier forms such as Bradt-Peters [17], the Wilson et al. geometric formula used to estimate interaction lengths can be applied to hydrogen targets as well as higher-A materials. These estimates are typically found to be accurate to within 10% or better, and the level of agreement tends to be similar (i.e., on the order of 10%) when comparing the measured charge-changing cross sections to more complex models such as NUCFRG2 [18], PHITS [19], etc.

III. DATA ANALYSIS

Our analysis methods have been described previously (see references [13] - [5]), but we provide additional details here as some aspects of the analysis (in particular, the analysis of light fragments using small-acceptance detectors) were not covered in the earlier articles.

As before, the CERN library program PAW [20] is used to perform most of the analysis. In the first step of data processing, the binary raw data are converted to a PAW-readable format and calibration constants are applied to convert the recorded pulse heights to deposited energy values. The cuts and histograms are made in PAW. The initial event sample is selected by requiring a single primary beam ion to have been recorded in the detectors placed upstream of the target. For each detector pair placed downstream of the target, a scatter plot is made showing the correlations between the ΔE in each, and a cut contour (in some cases, multiple contours) is drawn to select only events with well-correlated pulse heights; this removes events that manifest one or more well-know artifacts seen in the pulse-spectra recorded by these types of detectors, including edge hits or other causes of incomplete charge collection, and fragmentation occurring within the detector itself. For the small-acceptance analysis, described in more detail below, we select those events in which the charge of the leading (or most forward-produced) fragment cannot be determined by the large-acceptance detectors, along with events corresponding to the two or three lightest fragment species that can be resolved at large acceptance.

A. Large Acceptance Analysis

Examples of the correlation cuts in a large-acceptance detector pair are shown in Figures 4a (left) and 4b (right). Three cut contours are defined: the first selects events in the range from the lowest ΔE values up to those corresponding to fragments a few charge units below the primary; a second overlaps the high end of the first, and includes the remaining fragments; and the third selects ions of the primary species. There is no overlap of the second and third cuts. Figure 4a shows, for 650 MeV/nucleon ^{40}Ar on a polyethylene target, a realistic version of the first of the three contours; the second and third contours shown in this figure are "first pass" attempts that are further refined when we narrow the region of interest to be that containing the primary ions and the heaviest fragments, as in Figure 4b, where more realistic cut contours are shown. There is clearly a degree of subjectivity involved in drawing the contours, and in particular, varying the contour that defines the surviving primary ions affects the cross section results. Essentially, the contours define selection efficiencies, i.e., $N_{pass}(Z) = N_{true}(Z)\varepsilon(Z)$, where $N_{pass}(Z)$ is the number of events corresponding to a particular charge Z that are within the cut contour, and $N_{true}(Z)$ is the "real" number of such particles. Ideally, the contours would be drawn so as to make all values of $\varepsilon(Z)$ equal, in both target-in and target-out data. However, this ideal case cannot be realized in practice, with the result being that the drawing of the cut contours becomes a source – in some cases, the dominant source – of systematic error. We return to this point below.

A typical large-acceptance fragment charge spectrum is shown in Figure 5 for the same ^{40}Ar data set that was used to produce Figures 4a and 4b. Peaks are clear for charges as low as 10, with indications of peaks for charges 8 and 9, and no structure below charge 8. It could be argued that the charge 8 peak in this plot is significantly contaminated by background from high-multiplicity events with leading fragments having charges less than 8. This is checked explicitly in the small-acceptance analysis, where charge 8 and 9 fragment cross sections are also obtained and corrected for acceptance. If there were considerable background under the large-acceptance charge 8 peak, we would expect the small-acceptance (corrected) cross sections to be systematically smaller than the corresponding measurement at large acceptance. No such effect is observed, however, indicating that the background under the charge 8 peak is small.

TABLE I: Detector pairs and angular acceptances placed downstream of the target location for the experiments reported here. The angular acceptance is the half angle of the cone defined by the center of the target and the edge of the detector's active area. Beam energies are at extraction. The detector types (PSDs, 3 mm thick and 5 mm thick) are described in the text.

Ion Species	E_{beam} (MeV/nucleon)	Pair 1	Pair 2	Pair 3
^{35}Cl	650, 1000	PSD1 5.7°	5mm1/2 4.5°	3mm1/2 1.0°
^{40}Ar	290	PSD1 12.5°	5mm1/2 8.3°	3mm1/2 1.1°
^{40}Ar	400	5mm1/PSD1 6.7°	3mm1/2 2.5°	3mm3/4 1.2°
^{40}Ar	650	3mm1/2 7.0°	PSD1 8.8°	5mm1/2 1.8°
^{40}Ar	650	PSD1 12.5°	5mm1/2 1.9°	3mm1/2 0.9°
^{48}Ti	1000	PSD1 8.9°	5mm1/2 4.3°	5mm3/4 1.3°

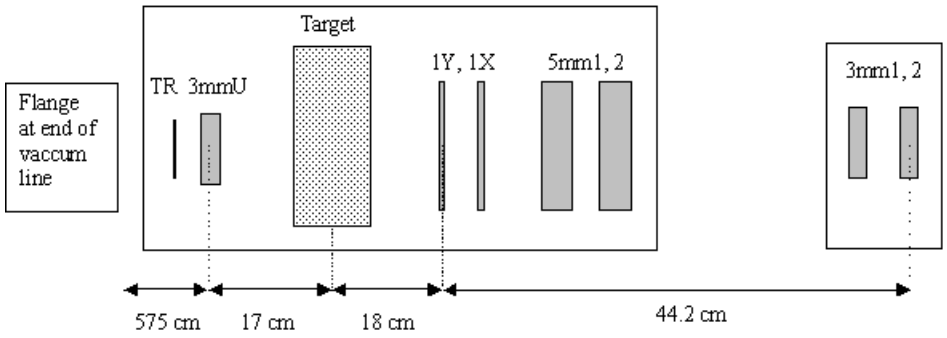

FIG. 1: Schematic diagram of the beamline configuration for the ^{35}Cl beam experiment. Spacing between detectors is 2 cm unless otherwise noted.

B. Small Acceptance Analysis

For a given run, the full sample of events in which the primary ion fragmented in the target is determined in the large-acceptance analysis, as explained above. A subset of these events is then analyzed in a small-acceptance detector pair. Most of the events in the chosen subset are those in which the ΔE in the large-acceptance detectors is in the unresolved portion of the spectrum. The remainder of the events in the subset are those in which the charge as determined by the large-acceptance detectors is at the low end of what can be resolved. An additional cut is applied, requiring well-correlated signals in the downstream detector pair. This cut removes events in which the fragment interacted in one or the other of the downstream detectors, and events in which one detector or the other spuriously recorded an incorrect ΔE. Figure 6 shows the small-acceptance (1.5°) charge spectrum for the same data set as was used to make Figure 5. The charge 8 and 9 peaks, which are quite marginal at large acceptance, emerge clearly at small acceptance, as do many others.

Structure is apparent in several of the fragment peaks in Figure 6. The charge 6 and 8 peaks are good examples of the phenomenon. For each, there is a relatively large peak close to the integer value (near 5.9 and 8.0, respectively), with a subsidiary peak or shoulder about 0.2 charge units above the main peak. As in previous work [14], we attribute the subsidiary peaks to the detection of one or more non-leading light fragments in coincidence with the leading fragment. The subsidiary peaks are typically in locations that are consistent with the detection of a helium fragment in coincidence with the leading fragment. For instance, the detected charge for an O and He fragment in coincidence, both at beam velocity, would be $\sqrt{68} \approx 8.25$.

The method used to determine the charge scale, in which a second-order polynomial is fit to several of the peaks in the ΔE plot, and the fit parameters are then used to obtain Z as a function of ΔE for each event, is imperfect, and as a result several peaks are offset compared to the expected integer values. This was noted above for charge 6, and it is also the case for some charges below 6. (The extreme low end of the spectrum is also the region where differential non-linearity in the analog-to-digital converter would have an effect, tending to push the charge 1 peak to a value smaller than the nominal 1.0.) The charge 5 peak appears at 4.9, charge 4 at 3.8, and charge 1 at 0.8. The offset is not global: the charge 2 peak appears at 2.0, and there is a small peak at 3.0. The small differences between measured Z and "true" Z do not affect our ability to interpret the peaks.

The presence of peaks near 1.3, 2.7, and 3.5 may seem surprising at first glance, but most likely these are due to coincidental detection of, respectively, a pair of charge

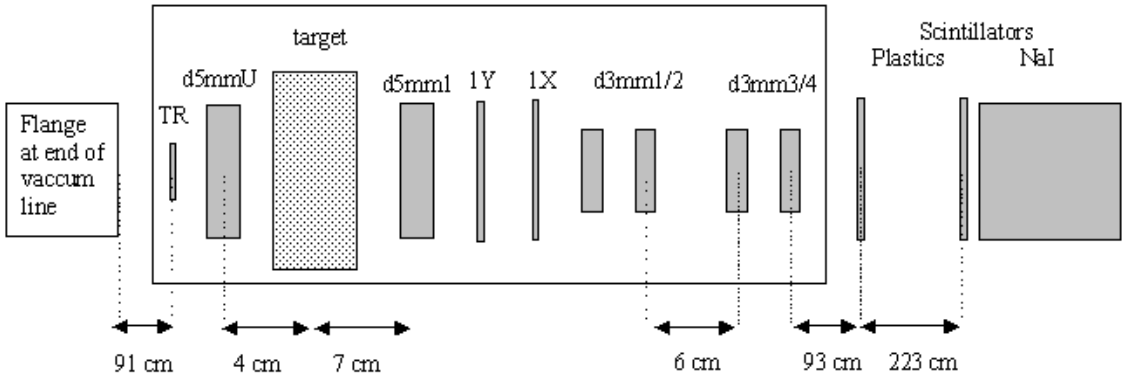

FIG. 2: Schematic diagram of the beamline configuration for the 400 MeV/nucleon ^{40}Ar beam experiment. Spacing between detectors was 2 cm unless otherwise noted.

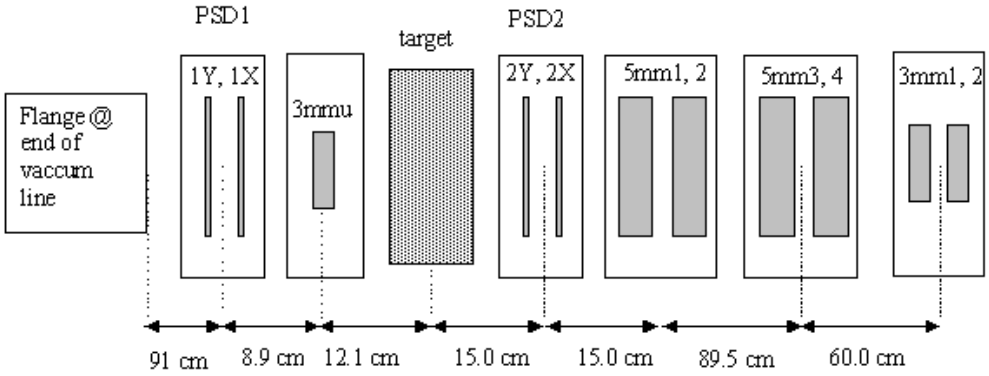

FIG. 3: Schematic diagram of the beamline configuration for the Ti beam experiment.

1 fragments (expected to appear at 1.4), a pair of charge 2 fragments (expected to appear near 2.8), and three charge 2 fragments (expected to appear at 3.5). It is possible that the peak near 3.5 also contains contributions from events with He and Li fragments in coincidence.

It is difficult to accurately judge by eye, or even with a multiple-Gaussian fit, how many of the events in the charge 2.5 to 3.1 region are due to Li fragments and how many are due to He fragment pairs, but it is clear that the latter dominate. This observation, along with the subsidiary peaks observed with heavier leading fragments, clearly show that helium fragments are copiously produced in these interactions. It is notable that the peaks for charge 2 fragments and pairs of charge 2 fragments are considerably more populated than the corresponding peaks for charge 1. However, it should be pointed out that projectile-like hydrogen fragments are probably produced at least as copiously as helium fragments, but they are less apparent in Figure 6 because they are harder to detect in these experiments. Particles with charge one, whether they are protons, other isotopes of hydrogen, or pions, go undetected if one or two deposit energy in coincidence with heavier fragments, and, because their angular distributions are broader than those of higher-Z fragments, there is a relatively low geometric efficiency for seeing them in the small-acceptance detectors. A fuller understanding of H and He fragment production cross sections may provide critical tests for fragmentation models. The experiments described here are not optimized for this purpose, but even so there is considerable information – beyond the scope of this work – that can be extracted from the existing data sets. Also, new experiments can be designed to address these questions in the future.

For these beams, there is significant ambiguity in the interpretation of the peaks below charge 5. For instance, the peak near charge 4 can be due to single Be fragments, or pairs of Li fragments in coincidence, or four He fragments in coincidence. The charge 3 peaks are similarly ambiguous between single Li fragments and pairs of He fragments. Similar combinations can be formed to make higher-charge peaks ambiguous, but for the most part these require improbable modes of fragmentation and/or very high detected multiplicities in detectors with small

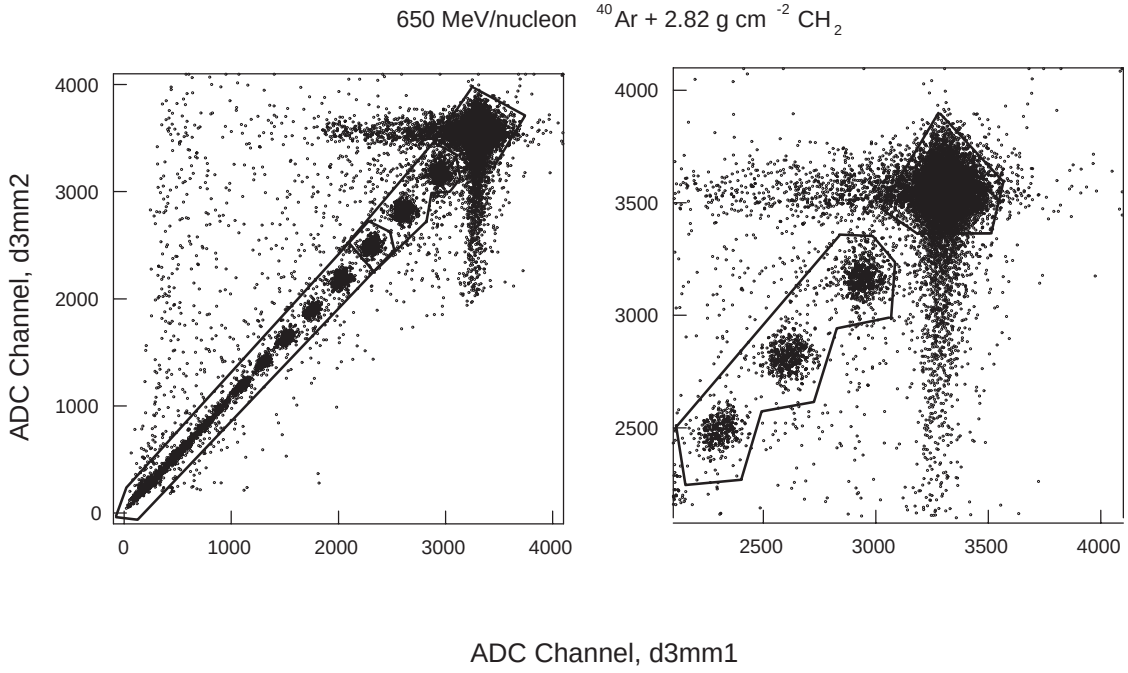

FIG. 4: Left, Figure 4a, cut contours on the scatter plot covering the full range of signals. The data are from a run with the 650 MeV/nucleon ^{40}Ar beam incident on a 2.82 g cm^{-2} polyethylene target. The two contours that define the primary and heaviest fragments are made crudely in the full-scale plot, and are refined by zooming in, as in Figure 4b on the right.

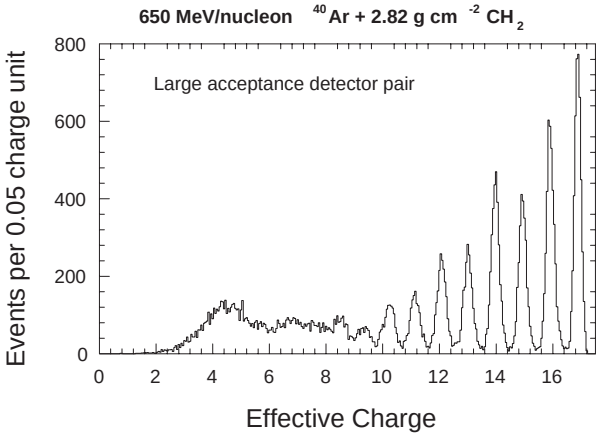

FIG. 5: Charge spectrum of fragments detected at large acceptance for 650 MeV/nucleon ^{40}Ar on a polyethylene target. The events that populate this histogram in the region of charge below about 11.5 were used to make the histogram in Figure 6.

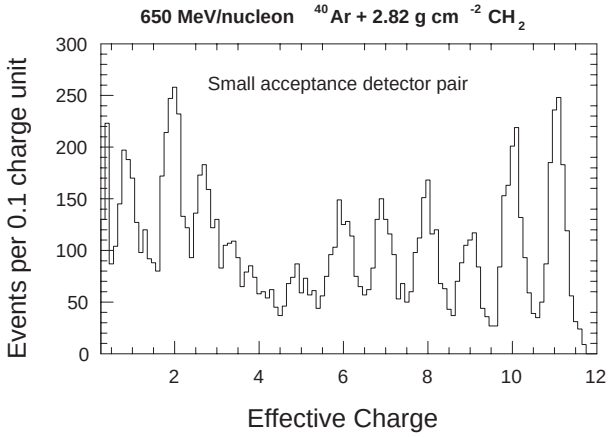

FIG. 6: Charge spectrum of light fragments from 650 MeV/nucleon ^{40}Ar incident on a polyethylene target. Events with fragments having charge up to 11 are included here, so that the cross sections for several fragment species (8 through 11 in this case) are measured in both large- and small-acceptance analyses. The overlapping measurements are used to adjust the momentum width parameter σ_0 in the acceptance model.

acceptance, which is statistically unlikely. We therefore take fragment charge 5 to be the lightest fragment species that is unambiguously identified in these data.

C. Correction Factors

In analyzing any given experiment, the analysis procedures are performed with as high a degree of consistency as possible for all runs, including those in which no target was on the beamline. These are taken for every experiment, and are analyzed in the same manner as the data taken with targets. The results are used to estimate the effects of fragmentation that unavoidably occurs in air gaps, entrance windows, and detector dead layers. The

probability, typically 1 to 2% in these experiments, for losing a primary ion to such an interaction is determined from the target-out data and is applied as a correction to the number of primaries in the target-in data, increasing their relative number. Probabilities for observing particular fragment species in the target-out data are subtracted from the target-in data, decreasing their relative numbers. Additional corrections to the fragment counts are applied to compensate for the effects of multiple interactions in the target; these are calculated using a Monte Carlo program which contains cross sections from the NUCFRG2 model. Corrections are also applied corresponding to the probability for an ion of a given species to survive to the depth in the stack at which it is measured. These can be significant, depending on the depths of both the target and the stack in a particular run, and are obviously smallest for the large-acceptance detectors closest to the target. The correction factors have associated uncertainties that must be taken into account when estimating the systematic errors in the cross sections.

Projectile fragments tend to retain the forward momentum of the primary and to receive fairly small transverse momentum in the collisions, resulting in strongly forward-peaked angular distributions. Also, multiple scattering angles are typically quite small at these energies, and have a negligible effect on the large-acceptance spectra. The large-acceptance data also require the smallest corrections for losses in the detectors and intervening materials, and are therefore used to obtain the charge-changing cross sections, σ_{cc}, and fragment cross sections for as many species as can be resolved. For the Cl beams and in some instances the Ar beams, the lowest resolvable fragment species is O, charge 8; for the Ti beam and other instances with Ar beams, fragments down to Ne, charge 10, can be resolved at large acceptance.

IV. SYSTEMATIC UNCERTAINTIES

As discussed in previous work, we take a conservative approach to assessing systematic errors. Since statistical errors are generally small in these experiments, the systematic uncertainties – with many distinct contributions – dominate the total. Our primary method of estimating the uncertainties is to obtain at least two data sets with the same beam ion/energy/target material combinations, varying only the target depth. Cross sections obtained at different depths of the same material must, after all corrections are applied, be equal. The variations that are observed are measures of the systematic uncertainties arising from the measurement and analysis procedures.

An additional source of systematic uncertainty in this and similar measurements is a lack of precision in the determination of the beam energy at the point of interaction. We determine the target-center energies by assuming a monoenergetic beam at the vacuum exit and calculating energy loss in all materials up to the midpoint of the target using a standard calculation based on a precise implementation of the Bethe-Bloch formula. These calculations take account of the upstream detector mass (typically 0.30 to 0.33 cm of silicon), air gaps, and any windows that may be present. The variations in target-center energy depend on the energy of the beam at extraction, the materials interposed between the end of the vacuum line and the target, and both the composition and depth of the target. In presenting the cross section results, we use target-center energies, but the fact that the interactions occur in ranges of energies should be kept in mind. Because the energy dependence of fragmentation cross sections at these energies is modest, this is expected to be a small effect, probably smaller than the other systematic sources of uncertainty.

With limited beam time and many target materials to be measured, one can only obtain reasonable fragment statistics by using targets whose depths represent at least a few percent of an interaction length. With high-A targets like Sn and Pb, ionization energy losses per unit interaction length are relatively large compared to low-A materials. In order to keep the beam energy approximately constant throughout the depth, high-A targets must therefore be kept thin, yielding poorer fragment statistics and larger relative systematic errors on the cross sections compared to lower-A targets such as C and Al. The increased relative systematic error arises for reasons discussed in the following section.

A. Charge-Changing Cross Section Uncertainties

The largest source of systematic uncertainty on any given charge-changing cross section is the definition of the cut contour (see Fig. 4 above) used to define the samples of surviving primaries and heaviest (ΔZ = 1 or 2) fragments. The worst cases are the target-out and very thin target runs, in which the low-ΔE tail of the primary distribution can substantially overlap the distribution of events with fragments one charge unit lower. Even in data sets with reasonable separation of clusters in the scatter plot (e.g., Fig. 4b), there are always some events that fall in the gap between the densest parts of the clusters. To reflect the uncertainty in the exact placement of the cut contours, we assign a systematic error to the fraction of surviving primaries, f, after correcting for losses as determined by the target-out data. The error assigned is determined by comparison of results obtained after repeated "best guess" attempts to draw the contours and typically correspond to an uncertainty in the third decimal place of the surviving primary fraction, 0.005 or smaller. Since the charge-changing cross section goes as the logarithm of f, to first order it is proportional to $(1-f)$ (a good approximation for thin targets), so that $\Delta\sigma_{cc}/\sigma_{cc} \propto \Delta f/(1-f)$. Since Δf is, for any given experiment, approximately constant, the uncertainty is obviously largest when f approaches 1, which is the case

for thin targets.

Additional sources of uncertainty include those arising from the model used to estimate the losses due to nuclear interactions in the detectors and the limited precision of the target areal density measurements. Each of these sources are estimated to contribute relative errors on the order of 1% to the charge-changing cross sections. For thin targets, these errors are much smaller than the uncertainty associated with the cut contour, but they can be important for thicker targets. Final determination of the systematic error on a given charge-changing cross section is made when the results from multiple targets are combined. To start, the weighted average, errors, and a χ^2 are computed. The systematic error on each measurement is taken to be that arising from the cut contour definition. If χ^2 is greater than 1.0 per degree of freedom (= number of data sets - 1), then an additional systematic error is added in quadrature to the starting error, and incremented upward in steps of 0.1% relative error until χ^2 is less than 1 per degree of freedom. In practice, it is rarely necessary to increase the uncertainty in this way, as the cut contour uncertainties are chosen so conservatively.

B. Uncertainties on Fragment Cross Sections at Large Acceptance

For each data set, the uncertainty on the charge-changing cross section is propagated into the fragment cross sections, and added in quadrature to the statistical errors (which are much larger for the counts of fragments than they are for the counts of primaries, given the modest target depths typically used). When data sets are combined, we again allow for the addition in quadrature of additional systematic uncertainties sufficient to bring the total χ^2 (summed over all fragment species) to less than 1.0 per degree of freedom. When considering the fragment cross sections, it is much more common for additional uncertainties to be required at this step than for the charge-changing cross sections. We attribute this to the ambiguities associated with the definition of the cut contour that defines the sample of the heaviest fragments (see Fig. 4b), and with the proper counting of events in the "valleys" between fragment peaks.

C. Fragment Cross Sections at Small Acceptance

As in previous work with a similar beam, ^{28}Si [4], the acceptance correction that is applied for losses due to the fragment angular spreads must be considered as an additional source of systematic uncertainty for the light-fragment cross sections. There, we compared large- and small-acceptance measurements of cross sections for the fragment species that were the lowest resolvable at large acceptance. We histogrammed the ratios of cross sections at the two acceptances were taken, and found a mean of 0.99 with a standard deviation of 6%, which was taken as a systematic error and added in quadrature to the others. Here, we evaluate the differences in the large- and small-acceptance measurements on a case-by-case basis. Errors are adjust upward as needed to obtain χ^2's of 1 or less per degree of freedom. The additional uncertainties are typically around 5%, similar to those found in the ^{28}Si beam data. This extra uncertainty accounts for reasonable variations in beam parameters (spot size and divergence), as well as variations in the model parameter σ_0, and in our understanding of the exact active areas of the detectors.

V. RESULTS

A. Charge-Changing Cross Sections

Table 2 and Figure 7 show the charge-changing cross section results. In the figure, the hydrogen-target cross sections and errors have been multiplied by a factor of 2.5 in order to compress the vertical scales. The figure has been split into two plots, with results from the lower-energy beams on the left and the higher-energy results on the right. The 400 MeV/nucleon ^{40}Ar data have been omitted in order to make the plot less cluttered; the 400 MeV/nucleon data points are, in all cases except that of the H target, within the errors on the 290 MeV/nucleon ^{40}Ar data. NUCFRG2 and PHITS predictions are also shown in Table 2, and NUCFRG2 results are shown in Figure 7. Model comparisons are discussed below.

The energy-independent reaction cross section formula of Wilson et al. [16] is given by $\sigma = \pi r_0^2(A_t^{1/3} + A_p^{1/3} - b - (1/A_t) - (1/A_p))^{2/3}$, with r_0 the nucleon radius and $b = 0.2$ an empirically-determined parameter related to transparency. The cross sections given by this formula are slightly larger than the charge-changing cross sections, since a small fraction of the interactions result in neutron stripping only. With this and similar forms, for a fixed target mass A_t, reaction cross sections monotonically increase with increasing projectile mass A_p. Since we only measure charge-changing cross sections and not total reaction cross sections, we are not testing this point directly, but we can say that with regard to charge-changing cross sections, the monotonic increase with A_p does not hold. This is seen most clearly in the hydrogen target data: at 290 and 400 MeV/nucleon, the ^{40}Ar charge-changing cross sections are smaller than those for the higher-energy ^{35}Cl beams at 650 and 1000 MeV/nucleon. The trend is also seen, albeit with less statistical significance, for C targets. For heavier targets, the cross sections for these four beams tend to be equal within the uncertainties. Thus, for beams with such similar mass numbers, differences in energy (and/or the z component of isospin) appear in some cases to have a greater effect on the charge-changing cross sections than do the small differences in A_p. Nonetheless, it is entirely possible that inclusion of the non-charge-change

cross sections (e.g., neutron-stripping) would bring the data into agreement with the purely geometric form.

The three measurements of ^{40}Ar in Table 2 suggest a mild energy dependence of the H-target cross sections. A similar trend was observed in ^{28}Si beam data in the energy range from 290 to 1200 MeV/nucleon [4], and for other beams by Webber et al. [10] and Chen et al. [21]. The 650 and 1000 MeV/nucleon ^{35}Cl beam data in Table 2 are mutually consistent within the uncertainties. (The same can be said of the two highest-energy measurements of ^{28}Si in Ref. [4], at 765 and 1147 MeV/nucleon.) We can also make limited comparisons of different beam ions at a given energy – 650 MeV/nucleon Ar vs. Cl and 1000 MeV/nucleon Ti vs. Cl. The expected A_p dependence is seen in almost every instance, though the uncertainties preclude definitive comparisons for 650 MeV/nucleon data and the Cu, Sn, and Pb targets.

The Pb-target cross sections obtained here are all larger than our previously-reported cross section for 1.05 GeV/nucleon ^{56}Fe beam on a Pb target [13]. That value, which was based on a measurement made with a single target, was reported as 4185 ± 107 mb, but subsequent to publication many additional data sets have been gathered and our analysis techniques have been refined. A reanalysis of the Pb-target data set reported in Ref. 13, combined with the newer data obtained with the same beam on other Pb targets, yields a revised value of 4554 ± 133 mb, nearly 9% larger. This revised value is, as expected from geometric cross section considerations, larger than the cross sections for Pb targets with ^{35}Cl and ^{40}Ar beams, and is within uncertainties of the value obtained with the ^{48}Ti beam.

1. *Comparison to Previous ^{40}Ar Measurements*

Three previous articles [6, 8, 21] have reported ^{40}Ar cross sections on hydrogen targets at energies similar to those presented here. Webber et al. [6] and Iancu et al. [8] also report cross sections for ^{40}Ar on carbon targets. The charge-changing cross sections from these experiments are all shown in Figure 8, plotted against beam energy at the center of the target. For the hydrogen-target results, one can draw a smooth curve through the low-energy points up to the Webber et al. point at 521 MeV/nucleon; from that point on up, there is no evidence of energy dependence. For carbon targets, there is mild disagreement, a little less than 4%, between our result and that of Iancu et al. around 360 MeV/nucleon. This 48 mb difference is slightly beyond the combined errors on the two measurements. Our data point at 248 MeV/nucleon is consistent with either of the data points at 360 MeV/nucleon and therefore does not help resolve the question of which of the two is more reliable. Regardless of the disparity at 360 MeV/nucleon, the carbon-target data show a trend that is qualitatively similar to, though less pronounced than, that seen in the hydrogen-target cross sections, with a rise from the lowest energy to 521 MeV/nucleon and little or no energy dependence from 521 to 792 MeV/nucleon.

We can compare cross sections for H, C, Al, Cu, and Pb targets obtained in this experiment with those obtained by Iancu et al. A straightforward calculation of χ^2 gives a value of 6.4 for the 5 measured points, indicating reasonable agreement. This suggests that the systematic error estimates, though on the conservative side, are reasonable. On average, the cross sections obtained here are lower by about 1.3%, but this is within the systematic uncertainties. We can also obtain a comparison in the vicinity of $A_t \approx 110$; Iancu et al. used a target of Ag ($A_t = 108$) while we used Sn ($A_t = 119$). Our ^{40}Ar data can be fit quite well by a power law form, $\sigma_{cc}(A_t) = 441.4A_t^{0.4226}$. This predicts a value of 3193 ± 66 mb for Ag, in excellent agreement with the value of 3221 ± 57 mb obtained by Iancu et al.

2. *Model Comparisons*

For reasons explained below, our model comparisons are focused on PHITS and NUCFRG2. PHITS is still in active development and is in many ways typical of large Monte Carlo codes in that it attempts to describe many physical processes, requires a sizable collaboration to maintain and improve the code, requires some expertise on the part of its users, and also requires considerable CPU time to yield results. NUCFRG2, in contrast, is analytic, is maintained by a small group, requires no expertise on the part of the user, and consumes far less than one CPU second on any modern computer to produce a list of cross sections for a given beam ion/energy/target combination. NUCFRG2 is fast because it does not transport particles – it only generates cross sections. This makes it suitable for inclusion in larger codes that do simulate transport [22]. And while the code described in Ref. 22 has proven to be extremely useful for certain purposes, it is a one-dimensional model and therefore of limited interest here.

3. *Comparisons to NUCFRG2*

The charge-changing cross sections predicted by the NUCFRG2 model for these beam/target combinations are shown alongside the experimental data in Figure 7 and Table 2. In the figure, the curve for 650 MeV/nucleon ^{35}Cl is difficult to see, as it is mostly covered by the curve for ^{40}Ar for A_t above 30. In general, the agreement is excellent for hydrogen targets, and good for carbon targets, but significantly worse for higher-A target materials. This is apparently due to model tuning based on the availability of proton-beam cross sections for many different targets [23]. In order to gain a better understanding of the systematic differences between the data and the model, in the following when we average over targets, we exclude hydrogen targets. It is clear

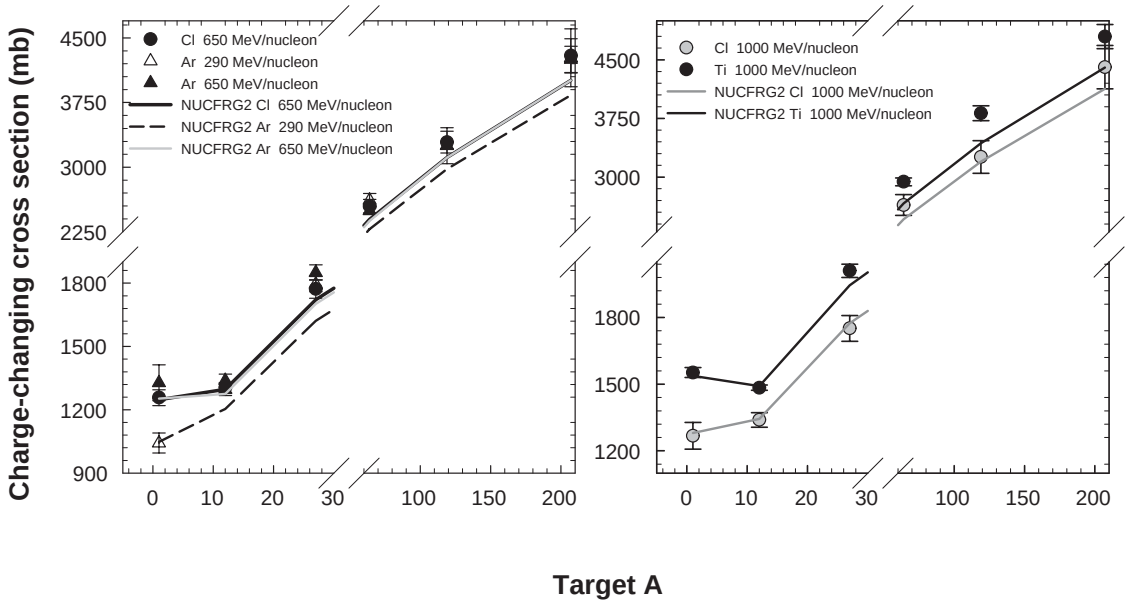

FIG. 7: Charge changing cross sections compared to NUCFRG2 predictions. In the figure on the left, results for 650 MeV/nucleon ^{35}Cl and ^{40}Ar beams are shown, along with 290 MeV/nucleon ^{40}Ar data. The figure on the right shows the results for the two 1000 MeV/nucleon beams measured here, ^{35}Cl and ^{48}Ti. In all cases the hydrogen-target data have been multiplied by a factor of 2.5 to compress the scales.

TABLE II: Measured charge-changing cross sections and uncertainties (top line of each section), NUCFRG2 predictions (middle line each section), and PHITS predictions (bottom line each section). Listed energies are for the extracted beams.

	H	C	Al	Cu	Sn	Pb
^{35}Cl	503 ± 15	1305 ± 23	1772 ± 44	2547 ± 79	3291 ± 126	4295 ± 196
650 MeV/nucleon	499	1297	1721	2395	3112	4007
	447	1288	1758	2536	3306	4252
^{35}Cl	507 ± 24	1339 ± 33	1751 ± 58	2643 ± 133	3257 ± 209	4406 ± 276
1000 MeV/nucleon	512	1343	1774	2461	3197	4129
	469	1335	1752	2508	3231	4172
^{40}Ar	417 ± 19	1295 ± 28	1795 ± 36	2616 ± 80	3249 ± 209	4269 ± 337
290 MeV/nucleon	419	1203	1621	2280	2977	3836
	352	1202	1681	2436	3259	4182
^{40}Ar	442 ± 23	1283 ± 31	1741 ± 49	2524 ± 39	3341 ± 69	4251 ± 104
400 MeV/nucleon	454	1216	1634	2296	3001	3871
	398	1194	1671	2426	3165	4154
^{40}Ar	531 ± 34	1338 ± 31	1850 ± 36	2495 ± 31	3252 ± 42	4249 ± 155
650 MeV/nucleon	501	1275	1701	2377	3110	4008
	467	1203	1657	2336	3085	4066
^{48}Ti	619 ± 16	1485 ± 21	2008 ± 37	2942 ± 59	3816 ± 105	4782 ± 174
1000 MeV/nucleon	615	1491	1945	2664	3433	4402
	561	1376	1785	2501	3269	4239

from Figure 7 that the model accurately reproduces the ^{35}Cl cross sections, particularly at 1 GeV/nucleon, but is less accurate for the other beams.

The lack of agreement for aluminum and (especially) heavier targets is similar to the trend seen when we compared NUCFRG2 calculations to ^{28}Si beam data [4]. The measured charge-changing cross sections tend to be larger than predicted, and the disparities tend to be larger for lower energies. The discrepancies found in the present study are larger in magnitude than those found with ^{28}Si beams. The ratios of measured to cross sections predicted by NUCFRG2 and PHITS are given in Table 3. The bottom row contains the weighted averages and errors averaged over the six beam ion/energy combina-

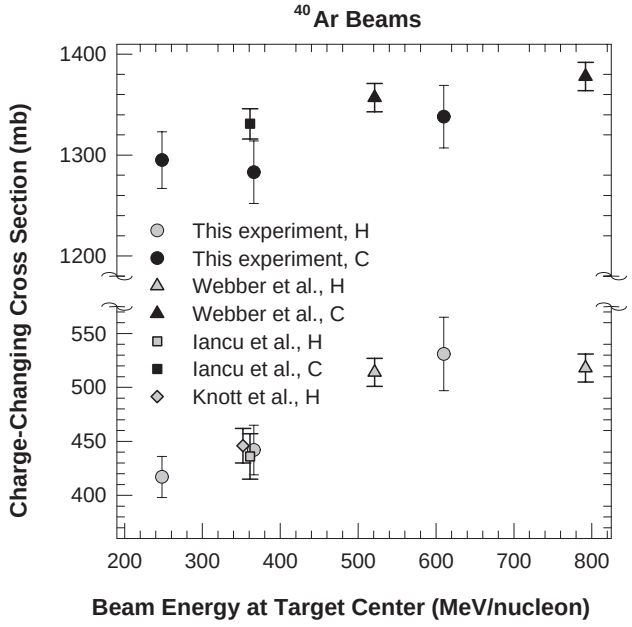

FIG. 8: Charge changing cross sections compared to previous experiments with ^{40}Ar beams at similar energies.

tions. Some systematic effects are readily apparent. In the ^{28}Si comparisons, the worst case, with target-center energy of about 270 MeV/nucleon, showed a discrepancy (averaged over the same target materials, but with hydrogen included) of 3.7%. In contrast, the worst case in these data, ^{40}Ar at 248 MeV/nucleon target-center energy, shows (with hydrogen excluded) a discrepancy in excess of 10%. The two next worst cases, both also with ^{40}Ar, at 366 and 610 MeV/nucleon, show 9.1% and 5.4% discrepancies, respectively. The best agreement is found for the 1 GeV/nucleon beams.

As can be seen in Table 2, disparities grow as target mass increases. The average ratio of measured to predicted cross sections for hydrogen is within uncertainties of 1.0, and the ratio for carbon is quite close to 1.0. However, for all other targets, the average ratios are all at least 1.055 and many standard deviations from 1.0. Ratios for the three highest-A targets are compatible within uncertainties, and so can be grouped. They are found to have a weighted average of 1.076 $\pm$ 0.006. Though the agreement for C and Al targets is somewhat better, they can be included, as they are in Table 3, in which case the average ratio is 1.056 $\pm$ 0.004.

Given that the largest disagreements are seen for the three ^{40}Ar beams, it might seem that this could conceivably be traced to the small neutron excess of this nucleus. However, ^{48}Ti has the same neutron excess, and NUCFRG2 successfully reproduces those cross sections to better than 2.5% on average. A general interpretation that is more consistent both with the data presented here and in other of our articles is that NUCFRG2 comes closer to the data at higher energies, where the cross sections approach energy-independence. In other words, in the low-energy region where the cross sections are varying, the model is less accurate than at higher energies where there is little or no variation. The highly relevant work done in this area by Tripathi et al. [24] subsequent to the creation of NUCFRG2 is apparently not included in the code, but perhaps should be.

4. Comparisons to PHITS

The PHITS Monte Carlo code was used to simulate several aspects of the experiment. Nucleus-nucleus collisions in PHITS are simulated by JAERI Quantum Molecular Dynamics (JQMD) [25]; nucleon-nucleus collisions are simulated by default by a Bertini-type model below 3.5 GeV/nucleon and by the Jet AA Microscopic Transport Model (JAM) hadron cascade model [26] above 3.5 GeV/nucleon. There are three different options for the calculating the nucleon-nucleon cross section when using the Bertini model in PHITS. Two parameterizations by Cugnon [27, 28] and one free p-p and n-n cross sections parameterized according to Niita et al. [26]. The nucleon-nucleon cross section described in ref. [27] is the default. For both types of collisions, the Generalized Evaporation Model (GEM) [29] is used by default to treat the evaporation stage of the reaction. It is possible to choose to simulate even nucleon-nucleus reactions with the JQMD model; however, this is not the default since the intranuclear cascade models are faster.

As in Ref. 5, a simplified simulation method was used in which the detectors were represented as voids corresponding to the actual volumes and positions of the silicon detectors, and particles were scored as they crossed these volumes with their varying acceptance angles. The reconstruction of events as seen by the detector was facilitated by keeping track of the PHITS-generated event number associated with each particle, and then, in a post-simulation step, merging these tracks into event records similar to those acquired in the experiment. Included in each event record are the number of tracks, the sums of the charge, mass, and LET (dE/dx in water) of the particles crossing the detector volume, and the charge of the highest-Z particle in the event (the leading fragment or the primary if there was no interaction). Either the summed charge squared or the summed LET serves as a reasonable proxy for the signal in a silicon detector. For each Monte Carlo run, two PAW ntuples were created per acceptance angle, one consisting of the event records and the other consisting of tracks (one entry per track). These can be used to cross-check the event records to make sure that the number of fragments of a given species is correctly counted. The Monte Carlo spectra can be analyzed in a manner analogous to (though much simpler than) that of the real data analysis to determine the generated charge-changing and fragment production cross sections. Where several corrections must be applied to the real data, only the correction for secondary interactions in the target is needed for the simulated data.

TABLE III: Ratios of measured charge-changing cross sections to predicted cross sections from NUCFRG2 and PHITS predictions. As explained in the text, PHITS has two options for modeling H-target interactions, Bertini and JQMD; results are shown for each. The energies are for the extracted beams.

E_{beam} (Mev per nucleon)	Beam Ion	H NUCFRG2	Other Targets NUCFRG2	H - Bertini PHITS	H - JQMD PHITS	Other Targets PHITS
290	^{40}Ar	0.995 ± 0.045	1.102 ± 0.014	1.185 ± 0.054	0.970 ± 0.040	1.071 ± 0.014
400	^{40}Ar	0.974 ± 0.051	1.091 ± 0.010	1.111 ± 0.058	0.938 ± 0.049	1.050 ± 0.020
650	^{35}Cl	1.008 ± 0.030	1.027 ± 0.012	1.125 ± 0.034	0.990 ± 0.030	1.009 ± 0.012
650	^{40}Ar	1.060 ± 0.068	1.054 ± 0.008	1.137 ± 0.073	1.029 ± 0.066	1.074 ± 0.008
1000	^{35}Cl	0.990 ± 0.047	1.008 ± 0.017	1.081 ± 0.051	0.971 ± 0.046	1.012 ± 0.017
1000	^{48}Ti	1.007 ± 0.020	1.045 ± 0.008	1.103 ± 0.029	1.015 ± 0.026	1.118 ± 0.010
Avg. this target		1.003 ± 0.016	1.056 ± 0.004	1.118 ± 0.017	0.991 ± 0.015	1.063 ± 0.004

In the upper histogram in Figure 9, we show a charge spectrum for simulated ^{40}Ar incident on a 2 g cm^{-2} aluminum target, produced using the event records. The quantity plotted is the square root of the sum of the squares of the charges passing through a volume corresponding to a large-acceptance detector. The histogram has been truncated on both axes – the Ar peak is not shown and the vertical scale is limited so that the least-populated regions of the plot are visible. The simulated spectrum has many features in common with the real data shown in Figure 5, including the lack of clear fragment peaks at the low end, and the shift of the well-defined peaks to above-integer values due to the contributions from non-leading fragments. Detector resolution effects are absent from the simulated spectrum, resulting in better definition of the peaks. Though certain details may be less than perfectly reproduced, on the whole the simulation yields a reasonable approximation of real data, at least for large acceptance.

Charge-changing cross sections predicted by PHITS are shown in Table 2, and average ratios of measured to cross sections predicted by PHITS are shown in the three rightmost columns of Table 3. From the above discussion, it is evident that NUCFRG2 accurately predicts H-target cross sections, is reasonably close for C targets, and is significantly further from the data for Al and heavier targets. For hydrogen targets, the accuracy of PHITS compared to the data is dependent on a user option to select either JQMD or a model based on Bertini (the default). Using the Bertini model, the PHITS predictions are furthest from the data for H targets, by an average of about 12% and with a worst-case disparity for 290 MeV/nucleon ^{40}Ar in excess of 18%. However, switching PHITS to use JQMD for hydrogen targets produces much better agreement with the data. Hydrogen appears [30] to provide the best shielding against heavy ions in the Galactic Cosmic Rays, and is likely to be used in flight applications, so it would seem appropriate that JQMD be considered the default for these applications. On the whole, PHITS appears superior to older models when comparing the measured fragment production cross sections to various models, as discussed below.

For targets other than H, PHITS appears to give about the same level of accuracy as NUCFRG2. Both models come closest to the data for the ^{35}Cl beams. For the ^{40}Ar and ^{48}Ti beams, the NUCFRG2 predictions are closer to the data at the higher energies, but PHITS predictions are systematically less accurate as beam energy increases. For both models, the ratios for targets heavier than hydrogen are in all cases greater than 1, indicating that the measured cross sections are larger than predicted. In a full-blown calculation of shielding against the GCR flux in free space, such systematic underestimates of the charge-changing cross sections will yield predictions of the dose behind shielding that err in the direction of being too high. Although in one sense this is conservative, it also carries the negative consequence of requiring extra shielding, and the accompanying steep penalty in launch costs, to achieve a given level of dose reduction. Thus even modest systematic errors in the cross sections could prove significant.

B. Fragment Production Cross Sections

Tables 4 through 9 show fragment production cross sections for the ^{35}Cl, ^{40}Ar, and ^{48}Ti beams, respectively. In all cases except the 290 MeV/nucleon ^{40}Ar data, cross sections are reported for fragment charges 5 and higher. Cross sections for the lightest reported species are obtained using small-acceptance detectors with corrections as described above. For the ^{35}Cl and the two higher-energy ^{40}Ar beams, the acceptance-corrected cross sections are for charges 5 through 7, and for ^{48}Ti, charges 5 through 9. For the 290 MeV/nucleon^{40}Ar experiment, several factors combine to make the resolution poor at low charge, even at small acceptance, as described in Section II above. Accordingly, only the large-acceptance results with fragment charges from 10 to 17 are presented for this beam.

In Figure 10, we plot the fragment cross sections divided by the charge-changing cross sections, for the highest energy available of each ion species. As in similar plots shown elsewhere [4, 5, 14], the plot emphasizes the differences between hydrogen and the other target materials, all of which yield quite similar results. The hy-

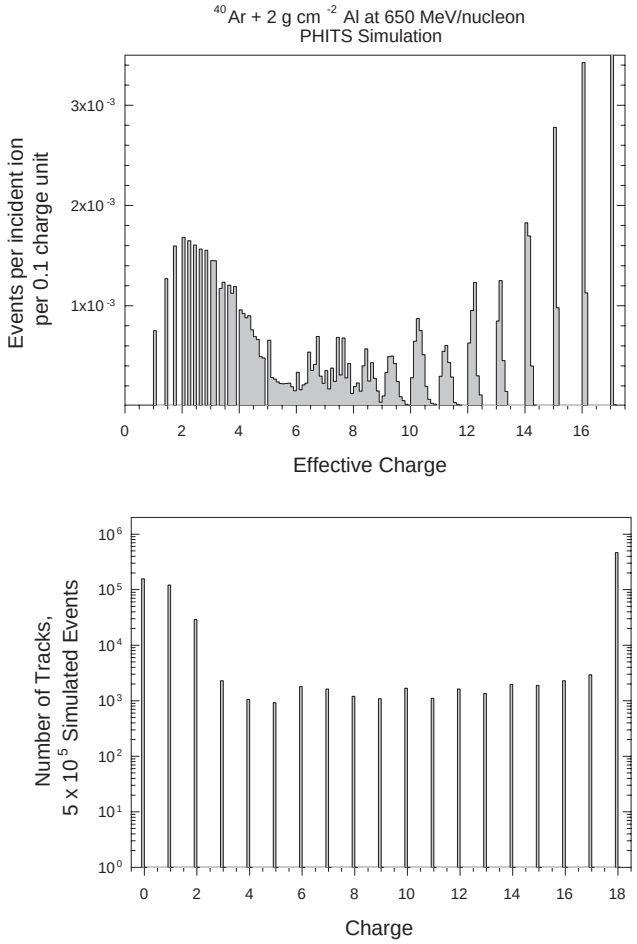

FIG. 9: Upper: Simulated fragment charge spectrum using PHITS with 650 MeV/nucleon ^{40}Ar incident on 2 g cm^{-2} of Al. The spectrum is derived from event records that approximate the detector signals seen in the experiment. Lower: Histogram of charge for all particles in the same simulation.

drogen data are markedly different, showing that much larger shares of the cross sections go into the smallest charge changes, and much smaller shares go into large charge changes. We note that, as usual, there are few instances in which the lines that are drawn to connect the points for a given target material cross one another for the targets other than H. The few exceptions tend to occur for relatively large charge changes, and are not significant in view of the uncertainties. The two exceptions that may be meaningful are for the $\Delta Z = 1$ cross sections in Pb for the 1 GeV/nucleon beams; these are enhanced by contributions from electromagnetic dissociation. We note that the fragment cross sections all reach minima for production of F (Z = 9); and, for targets other than H, the cross section shares for charges 5 to 8 are comparable to, or slightly larger than, those for charges 10 and 11. For H targets, the shares continue to fall, more or less monotonically, below charge 12.

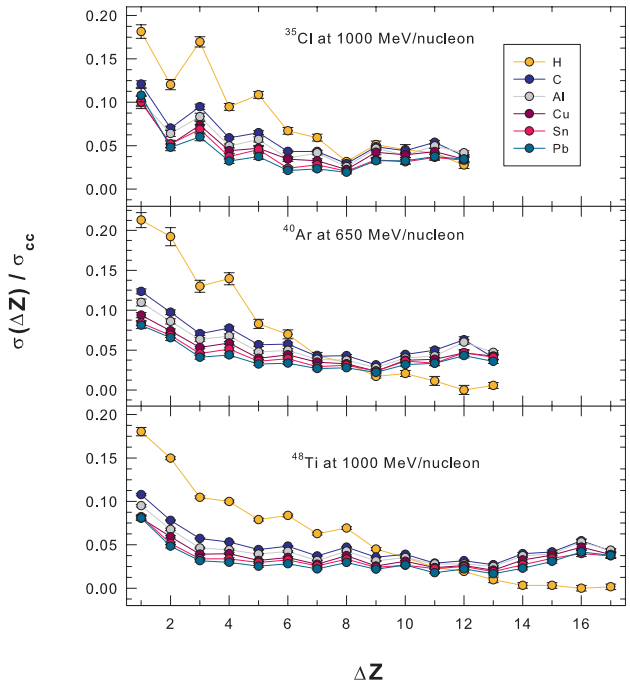

FIG. 10: Fragment cross sections normalized to the corresponding charge changing cross section, for 1 GeV/nucleon ^{35}Cl and ^{48}Ti beams, and the 650 MeV/nucleon ^{40}Ar beam.

1. *Odd-even Effect*

The ^{35}Cl data in Figure 10 show an especially strong odd-even effect, i.e., even-Z fragment cross sections are larger than the neighboring odd-Z cross sections. The effect is present, but not as obvious, for the ^{40}Ar and ^{48}Ti data. This is similar to the observations of Knott et al. and Iancu et al. in comparing ^{36}Ar to ^{40}Ar. Of particular note are the cases in the ^{35}Cl data for which the cross section for an even-Z fragment is larger than that for the next smaller charge change, since this behavior runs counter to the general trend of monotonic decrease with increasing ΔZ. These increases are seen for all targets for $\Delta Z = 3$ and 5, corresponding to the production of Si and Mg fragments. Compared to the ^{48}Ti and ^{40}Ar results, those for ^{35}Cl show a slightly different pattern, since production of even-Z fragments corresponds to odd-numbered charge changes.

To characterize the odd-even effect, Iancu et al. use the quantity

$$V\left(Z_f\right) = 2\sigma\left(Z_f\right)/[\sigma\left(Z_f+1\right) + \sigma\left(Z_f-1\right)]$$

where Z_f refers to the fragment species with charge Z. Figure 11 shows this quantity, calculated for the ^{48}Ti data on all but the Pb target. We have cross sections available for charges 5 to 21, so we can compute $V(Z_f)$ for charges 6 to 20. However, for the hydrogen target, the error bars are quite large below charge 11, so those data points have been omitted. The carbon and aluminum

TABLE IV: Fragment production cross sections for the 650 MeV/nucleon ^{35}Cl beam.

Z_{frag}	H target	C target	Al target	Cu target	Sn target	Pb target
16	101 ± 5	154 ± 4	185 ± 7	223 ± 10	311 ± 16	437 ± 26
15	69 ± 3	95 ± 3	111 ± 5	130 ± 7	165 ± 10	191 ± 15
14	95 ± 4	129 ± 3	152 ± 6	174 ± 8	184 ± 11	231 ± 17
13	53 ± 3	80 ± 2	94 ± 4	113 ± 6	124 ± 8	155 ± 12
12	54 ± 3	95 ± 3	110 ± 4	140 ± 7	127 ± 9	159 ± 13
11	31 ± 2	59 ± 2	68 ± 3	91 ± 5	94 ± 7	117 ± 10
10	27 ± 2	61 ± 2	72 ± 3	89 ± 5	107 ± 7	126 ± 10
9	13 ± 1	43 ± 2	53 ± 2	58 ± 4	69 ± 5	74 ± 8
8	19 ± 2	69 ± 2	80 ± 3	115 ± 5	115 ± 8	135 ± 11
7	17 ± 3	54 ± 4	67 ± 5	92 ± 8	102 ± 11	137 ± 16
6	13 ± 3	71 ± 5	93 ± 7	109 ± 9	120 ± 12	167 ± 19
5	4 ± 2	47 ± 3	51 ± 4	78 ± 8	91 ± 10	110 ± 15

TABLE V: Fragment production cross sections for the 1000 MeV/nucleon ^{35}Cl beam.

Z_{frag}	H target	C target	Al target	Cu target	Sn target	Pb target
16	92 ± 4	162 ± 5	178 ± 9	267 ± 16	326 ± 24	476 ± 34
15	61 ± 3	94 ± 3	112 ± 6	136 ± 10	169 ± 14	212 ± 17
14	86 ± 3	127 ± 4	146 ± 7	194 ± 12	224 ± 17	265 ± 20
13	48 ± 2	79 ± 2	87 ± 4	117 ± 8	122 ± 10	142 ± 12
12	55 ± 2	87 ± 3	100 ± 5	124 ± 9	148 ± 12	165 ± 14
11	34 ± 2	58 ± 2	62 ± 3	91 ± 7	78 ± 7	94 ± 9
10	30 ± 2	58 ± 2	73 ± 4	86 ± 6	91 ± 8	102 ± 10
9	16 ± 1	39 ± 2	45 ± 3	59 ± 5	67 ± 6	85 ± 8
8	26 ± 2	65 ± 2	82 ± 4	112 ± 8	110 ± 9	143 ± 12
7	23 ± 3	59 ± 2	68 ± 4	104 ± 8	102 ± 9	143 ± 15
6	21 ± 3	72 ± 3	87 ± 5	114 ± 9	119 ± 11	165 ± 17
5	14 ± 2	51 ± 2	73 ± 4	91 ± 8	108 ± 10	152 ± 16

data are found to be mutually consistent and have been combined to reduce both the clutter in the plot and the error bars, and similarly the copper and tin data have been combined. We do not include Pb target data here, since those cross sections may be influenced by the electromagnetic dissociation component.

Though $V(Z_f)$ is clearly a function of the fragment species, we can nonetheless group the odd and even charges together to get a rough estimate of the strength of the effect in the various data sets. The results are shown in Table 10. The $V(Z_f)$ values for $\Delta Z = 2$ fragments are excluded, since those are reduced by the presence, in the denominator, of the cross section for $\Delta Z = 1$, the favored channel for the most peripheral reactions; including $\Delta Z = 2$ $V(Z_f)$ values tends to obscure the effect. Some systematic dependences of $V(Z_f)$ on beam ion, energy, and target grouping can be inferred from the odd-Z and even-Z averages in Table 10. A further simplification can be made by taking the ratio of the average even-Z $V(Z_f)$ to the average odd-Z $V(Z_f)$; these values are shown in the bottom six rows of the table.

We consider the hydrogen-target results first. Due to the polyethylene/carbon subtraction method used to obtain the hydrogen-target cross sections, the uncertainties on the $V(Z_f)$ values are large compared to those for the other targets, and it is therefore difficult to find statistically meaningful trends in these data. To help clarify matters, we show in the top graph in Figure 12 the $V(Z_f)$ values for the data in Table 10, along with results derived from recently-published ^{28}Si beam cross sections

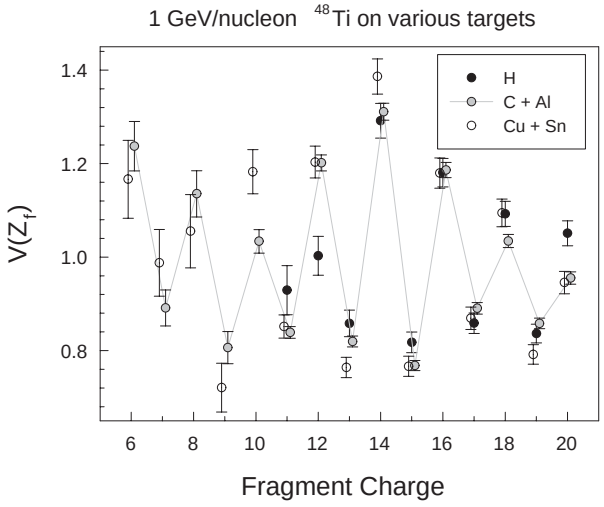

FIG. 11: Odd-even effect for the 1 GeV/nucleon ^{48}Ti beams on several targets.

TABLE VI: Fragment production cross sections for the 290 MeV/nucleon ^{40}Ar beam.

Z_{frag}	H target	C target	Al target	Cu target	Sn target	Pb target
17	136 ± 7	209 ± 2	239 ± 13	309 ± 12	375 ± 34	405 ± 47
16	103 ± 6	158 ± 5	190 ± 11	245 ± 10	288 ± 26	324 ± 36
15	65 ± 4	114 ± 3	129 ± 7	162 ± 7	159 ± 16	162 ± 22
14	53 ± 4	122 ± 3	142 ± 8	185 ± 7	175 ± 17	211 ± 25
13	27 ± 3	82 ± 3	98 ± 6	122 ± 5	146 ± 14	166 ± 20
12	15 ± 2	87 ± 3	103 ± 6	133 ± 6	132 ± 13	160 ± 19
11	7 ± 2	59 ± 2	67 ± 4	10 ± 5	115 ± 12	136 ± 17
10	2 ± 2	60 ± 2	83 ± 5	103 ± 5	98 ± 10	179 ± 20

TABLE VII: Fragment production cross sections for the 400 MeV/nucleon ^{40}Ar beam.

Z_{frag}	H target	C target	Al target	Cu target	Sn target	Pb target
17	128 ± 5	183 ± 5	210 ± 10	260 ± 6	333 ± 10	341 ± 13
16	101 ± 6	137 ± 4	156 ± 6	193 ± 8	224 ± 10	253 ± 15
15	65 ± 4	99 ± 3	117 ± 5	148 ± 6	162 ± 8	192 ± 11
14	59 ± 4	108 ± 4	122 ± 5	153 ± 6	184 ± 9	197 ± 12
13	31 ± 3	76 ± 3	88 ± 4	111 ± 5	122 ± 6	139 ± 9
12	22 ± 3	81 ± 3	90 ± 4	117 ± 5	122 ± 6	149 ± 9
11	15 ± 2	54 ± 2	65 ± 4	84 ± 3	111 ± 6	117 ± 7
10	7 ± 2	56 ± 2	68 ± 4	89 ± 4	102 ± 5	118 ± 7
9	4 ± 1	38 ± 1	42 ± 2	61 ± 3	72 ± 4	85 ± 6
8	6 ± 2	59 ± 2	74 ± 3	93 ± 4	108 ± 5	138 ± 8
7	5 ± 2	63 ± 2	78 ± 6	102 ± 5	119 ± 7	153 ± 10
6	1 ± 2	75 ± 3	92 ± 7	120 ± 6	151 ± 9	172 ± 12
5	1 ± 2	54 ± 2	82 ± 7	108 ± 5	118 ± 7	163 ± 11

[4] at five energies, and data from Chen et al. [9] using ^{40}Ca at three energies, to give us $T_z = 0$ points for comparison. We also include three data points for ^{56}Fe to further elucidate the behavior of $V(Z_f)$ for $T_z = -2$ beams. Of the ^{56}Fe results, one is based on published data [13], and two (those obtained with beam energies of 500 and 800 MeV/nucleon) are based on preliminary, unpublished results that will appear in a forthcoming article. Despite the considerable uncertainties, there appear to be three significant trends: First, the strongest effect is seen for $T_z = 0$ beams, the weakest for $T_z = -2$ beams, with $T_z = -0.5$ beam (^{35}Cl) in between. Second, in the $T_z = 0$ data, the effect decreases with increasing beam energy for ^{28}Si but appears to be approximately independent of energy for ^{40}Ca. Third, for the $T_z = -2$ beams, the average values are all mutually consistent, independent of energy, with a weighted average of 1.347 ± 0.021 and a χ^2 for energy independence of 5.7 for 6 degrees of freedom.

In the lower part of Figure 12, we show the results for the same beams as in the upper, but for combined carbon and aluminum target data. (The corresponding plot for combined copper and tin data is quite similar and is not shown here.) It is difficult to draw any conclusions regarding energy dependence from this plot. For ^{28}Si and beam energies up to 800 MeV/nucleon, there appears to be no significant dependence, but the effect appears to be weaker at 1200 MeV/nucleon than at the lower energies. Similarly, the ratio for ^{35}Cl drops at 1 GeV/nucleon compared to the 650 MeV/nucleon point. But for the $T_z = -2$ beam ions, the data appear, on first glance, to scatter with no obvious pattern. Closer examination shows what seem to be distinctly different trends for ^{40}Ar (weakening effect with increasing beam energy) and ^{56}Fe (energy independent or slight increase with increasing beam energy). The 1 GeV/nucleon ^{48}Ti point is, as it was for hydrogen targets, consistent with the result for ^{56}Fe at slightly higher energy.

In summary, the data show significant differences in the strength of the odd-even effect that depend on T_z and energy, and fairly weakly on the target. Contrary to the assertion of Knott et al., we find a non-negligible effect even for $T_z = -2$ beams. Hydrogen-target data for ^{28}Si, with $T_z = 0$, show an intuitively reasonable decrease of the effect with beam energy, again somewhat in conflict with the observations of Knott et al., who observed contrary behavior that they aptly described as "counterintuitive."

2. *Comparison to Previous ^{40}Ar Measurements with Hydrogen Targets*

With the addition of the present results, there are now seven measurements reported with ^{40}Ar on hydrogen targets at energies between 240 and 800 MeV/nucleon. In

TABLE VIII: Fragment production cross sections for the 650 MeV/nucleon ^{40}Ar beam.

Z_{frag}	H target	C target	Al target	Cu target	Sn target	Pb target
17	113 ± 5	164 ± 2	203 ± 8	234 ± 8	273 ± 10	345 ± 18
16	102 ± 6	131 ± 5	159 ± 6	185 ± 6	223 ± 9	278 ± 15
15	69 ± 4	94 ± 3	117 ± 4	133 ± 4	148 ± 6	174 ± 10
14	74 ± 4	104 ± 3	125 ± 5	147 ± 5	167 ± 7	186 ± 10
13	44 ± 3	76 ± 3	88 ± 3	99 ± 3	117 ± 5	138 ± 8
12	37 ± 3	77 ± 3	92 ± 4	110 ± 4	128 ± 5	143 ± 8
11	23 ± 2	56 ± 2	71 ± 3	87 ± 3	95 ± 4	114 ± 7
10	18 ± 2	58 ± 2	69 ± 3	82 ± 3	101 ± 4	118 ± 7
9	9 ± 1	41 ± 2	52 ± 2	59 ± 3	77 ± 4	94 ± 6
8	11 ± 2	60 ± 2	74 ± 3	93 ± 3	118 ± 5	135 ± 8
7	6 ± 3	65 ± 4	79 ± 4	96 ± 6	109 ± 10	142 ± 10
6	0 ± 3	83 ± 5	111 ± 5	116 ± 7	152 ± 13	183 ± 12
5	3 ± 2	53 ± 3	87 ± 4	106 ± 10	133 ± 11	152 ± 11

TABLE IX: Fragment production cross sections for the 1000 MeV/nucleon ^{48}Ti beam.

Z_{frag}	H target	C target	Al target	Cu target	Sn target	Pb target
21	113 ± 3	159 ± 2	191 ± 5	238 ± 6	314 ± 10	387 ± 16
20	93 ± 2	116 ± 1	136 ± 3	174 ± 4	197 ± 6	231 ± 10
19	65 ± 1	85 ± 1	93 ± 2	115 ± 3	129 ± 5	151 ± 7
18	62 ± 1	79 ± 1	89 ± 2	117 ± 3	129 ± 5	143 ± 7
17	49 ± 1	66 ± 1	79 ± 2	94 ± 3	113 ± 4	121 ± 6
16	52 ± 1	72 ± 1	85 ± 2	104 ± 3	124 ± 4	135 ± 7
15	39 ± 1	55 ± 1	64 ± 1	81 ± 3	98 ± 4	106 ± 5
14	43 ± 1	70 ± 1	86 ± 2	110 ± 3	128 ± 4	142 ± 6
13	28 ± 1	53 ± 1	63 ± 1	75 ± 2	92 ± 3	105 ± 5
12	22 ± 1	58 ± 1	71 ± 1	91 ± 3	101 ± 4	127 ± 6
11	15 ± 1	43 ± 1	56 ± 1	70 ± 2	86 ± 3	85 ± 6
10	12 ± 1	47 ± 1	56 ± 1	77 ± 2	95 ± 3	104 ± 7
9	6 ± 2	51 ± 3	50 ± 2	61 ± 6	73 ± 7	80 ± 7
8	2 ± 2	59 ± 2	75 ± 2	96 ± 8	103 ± 9	110 ± 9
7	2 ± 2	62 ± 3	79 ± 4	112 ± 9	131 ± 11	148 ± 11
6	0 ± 3	81 ± 3	107 ± 5	139 ± 11	152 ± 13	200 ± 14
5	1 ± 2	64 ± 3	88 ± 4	114 ± 10	142 ± 12	181 ± 13

comparing the data sets, it is important to note that we expect both real differences in the form of energy dependence in the cross sections, and artifacts caused by systematic differences between experiments. When the latter are comparable in magnitude to the former, it is difficult or perhaps impossible to separate the two.

Data from the different experiments are plotted together in Figure 13, for fragment charges 11 through 17, against target-center beam energy. For each fragment charge, a particular shading is chosen; and for each experiment a particular symbol is chosen. Data points for charges 17, 14, and 11 are solid; for 16 and 13, open; and for 15 and 12, gray. For the present experiment, data points are represented by circles; for Knott et al., triangles; for Iancu et al., squares; and for Webber et al., diamonds. As previously noted by Webber et al. [10], the cross sections for certain fragment species show energy dependence that exceeds the measurement errors, but there are also systematic effects of comparable magnitude. For instance, each cross section in the Z = 11 to 17 range measured by Knott et al. is higher than the corresponding cross section reported by Iancu et al. For charges 16 and 17, the present experiment at a similar energy agrees well with Iancu et al., but is in substantially better agreement with Knott et al. for charges 13 to 15. (Below charge 13, there is generally good agreement between all three experiments, with the exception of an apparent outlier in our data at charge 11.) We discuss the results in the 360 MeV/nucleon region in more detail below. Looking at the full energy range covered in Figure 13, it is clear that, in general the cross sections for the smallest ΔZ's (1 and 2 charge units) decrease slightly with energy, and those for the larger ΔZ's (4 charge units or more) increase with energy, particularly in going from about 360 MeV/nucleon to 521 MeV/nucleon.

Three of the data sets shown in Figure 13 are at almost identical target-center energies: Knott et al. at 357 MeV/nucleon, Iancu et al. at 361 MeV/nucleon, and the present experiment at 366 MeV/nucleon. (The average of the three energies is 361 MeV/nucleon.) Over

TABLE X: $V(Z_f)$ values, averaged for even- and odd-Z fragments, for each beam. Also shown for each beam is the ratio of the average even-Z $V(Z_f)$ to the odd-Z $V(Z_f)$. Data for different targets are grouped, as explained in the text.

Beam Ion	Energy (MeV/nucleon)	Averaged Quantity	H	C + Al	Cu + Sn
Ti	1000	Even-Z $V(Z_f)$	1.141 ± 0.016	1.153 ± 0.008	1.191 ± 0.015
		Odd-Z $V(Z_f)$	0.845 ± 0.011	0.833 ± 0.005	0.804 ± 0.010
Ar	650	Even-Z $V(Z_f)$	1.201 ± 0.062	1.191 ± 0.019	1.203 ± 0.020
		Odd-Z $V(Z_f)$	0.771 ± 0.035	0.802 ± 0.015	0.786 ± 0.015
Ar	400	Even-Z $V(Z_f)$	1.084 ± 0.079	1.216 ± 0.020	1.168 ± 0.022
		Odd-Z $V(Z_f)$	0.804 ± 0.047	0.749 ± 0.013	0.800 ± 0.017
Ar	290	Even-Z $V(Z_f)$	1.051 ± 0.086	1.327 ± 0.027	1.282 ± 0.038
		Odd-Z $V(Z_f)$	0.822 ± 0.053	0.793 ± 0.016	0.793 ± 0.022
Cl	1000	Even-Z $V(Z_f)$	1.377 ± 0.042	1.292 ± 0.024	1.237 ± 0.043
		Odd-Z $V(Z_f)$	0.687 ± 0.024	0.733 ± 0.013	0.719 ± 0.025
Cl	650	Even-Z $V(Z_f)$	1.370 ± 0.051	1.356 ± 0.021	1.316 ± 0.033
		Odd-Z $V(Z_f)$	0.688 ± 0.030	0.719 ± 0.012	0.711 ± 0.020
Ti	1000	Even/odd ratio	1.351 ± 0.026	1.385 ± 0.012	1.480 ± 0.026
Ar	650	"	1.557 ± 0.107	1.485 ± 0.036	1.531 ± 0.039
Ar	400	"	1.348 ± 0.127	1.625 ± 0.039	1.459 ± 0.041
Ar	290	"	1.278 ± 0.134	1.673 ± 0.048	1.616 ± 0.066
Cl	1000	"	2.003 ± 0.092	1.761 ± 0.045	1.721 ± 0.085
Cl	650	"	1.990 ± 0.115	1.885 ± 0.043	1.852 ± 0.070

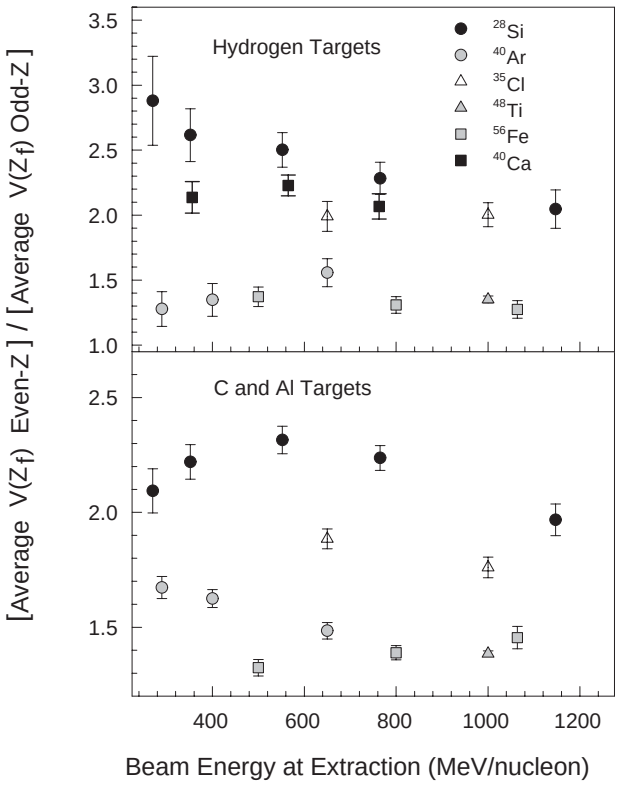

FIG. 12: Ratios of $V(Z_f)$ for even-Z fragments to $V(Z_f)$ for odd-Z fragments, with several beams for hydrogen targets (upper) and for combined data from carbon and aluminum targets (lower).

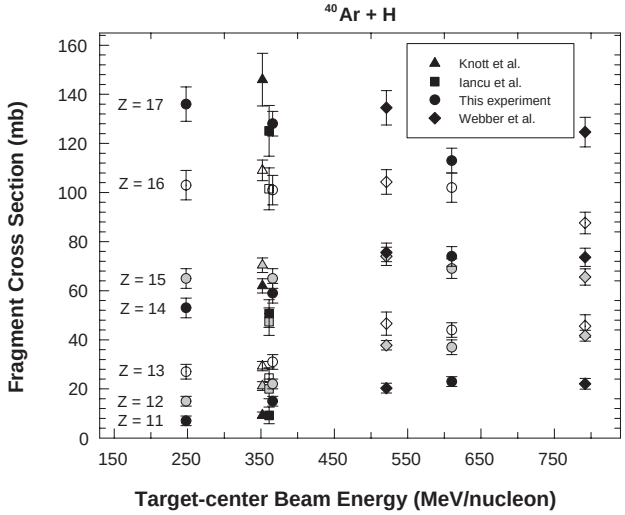

FIG. 13: Fragment cross sections for ^{40}Ar beams on hydrogen targets, reported by four separate experiments at seven distinct energies.

such a small range, there should be no significant change in the cross sections, and any discrepancies can be attributed to systematic effects in the data. Accordingly, for each fragment charge reported by the three groups, we calculated a weighted-average cross section, the error on the weighted average, and a χ^2 for the hypothesis that the data are all in agreement within the reported uncertainties. The calculation was performed for charges 9 through 17, the lower limit imposed by the Knott et al. data. This represents three measurements each of 9 separate cross sections, giving a total of 18 degrees of freedom. The summed χ^2 is 29.4, which is somewhat

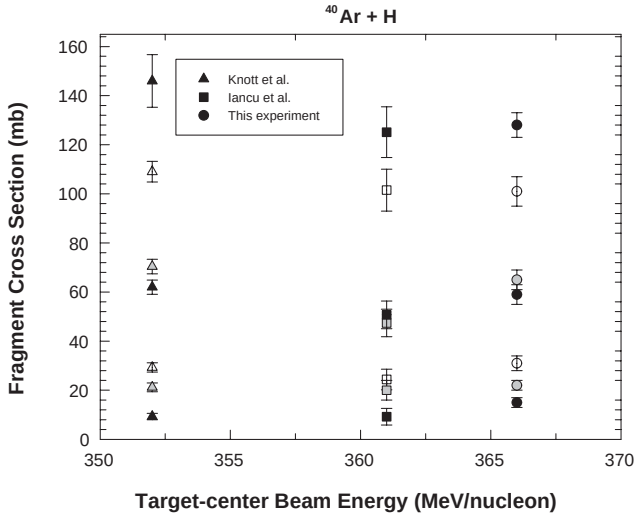

FIG. 14: Fragment cross sections for ^{40}Ar beams on hydrogen in a narrow energy range where three measurements have been made.

high compared the nominal value of about 1 per degree of freedom. However, a single point – the Iancu et al. measurement for charge 15 – contributes a χ^2 of 10.1 to the total. Removing this outlier from consideration, the χ^2 for the remaining data points is 19.3 for 17 degrees of freedom, indicating good agreement. The cross sections and averages are shown in Table 7, and a close-up of Figure 13, focusing on this region, is shown in Figure 14.

Since the data in the 352 to 366 MeV/nucleon range can be averaged with good confidence, it is reasonable to compare those cross sections to the measurement at 248 MeV/nucleon. For charges 15 through 17, the results are mutually compatible; but, as charge decreases, starting at Z = 14, the 248 MeV/nucleon cross sections are significantly smaller than those at 360 MeV/nucleon, and the differences grow as the fragment charge decreases. This is entirely consistent with the general behavior seen over the larger energy range in Figure 13.

C. Comparison to Other Data with Carbon and Heavier Targets

Previous measurements with ^{40}Ar beams incident on carbon targets have been reported by Webber et al. and Iancu et al., with the latter work also containing cross sections for Al, Cu, and Pb targets as in the present work. On the whole, agreement for carbon and heavier targets is not as good as for hydrogen targets, and there are consistent systematic differences between our results and those of Iancu et al.

For carbon targets, we can compare our data at 359 MeV/nucleon target-center energy to Iancu et al. at 361 MeV/nucleon, and our data at 580 MeV/nucleon to Webber et al. at 521 MeV/nucleon. Choosing energies relatively close to one another largely mitigates any energy dependence of the cross sections. A simple approach is to simply take the ratio of a particular cross section as measured by one experiment to the corresponding value from another experiment, and compute the average and standard deviation of the ratios. Using data from the present experiment as the denominator, when comparing to Iancu et al., we find an average ratio of 0.75 with a standard deviation of 0.15. Comparing to Webber et al., the average is 0.90 with a standard deviation of 0.13, substantially better agreement than at the lower energy.

For Al and Cu targets (for the moment excluding Pb), we can compare our data with the 400 MeV/nucleon extracted beam energy to the Iancu et al. results, and we obtain results that are very similar to those found for the carbon target. For Al, the average ratio as defined above is 0.76 with standard deviation 0.15; for Cu, 0.71 with standard deviation 0.14. In almost every single instance, the cross section obtained in the present experiment is larger than that obtained by Iancu et al. Comparing averages obscures the fact that the measurements tend to be in very good agreement for the smallest (1 and 2 unit) charge changes. Those cross sections generally agree within 5% between experiments, and the level of agreement appears to decrease with increasing charge change. For fragment charges 12 to 15, the average ratio is 0.75, but for charges 7 to 12, it is only 0.63. The worst cases are charges 7 and 8. These discrepancies are far beyond the systematic errors claimed by either experiment, and also far beyond any of the corrections that are applied in our data analysis. The trend suggests either a gross error lurking in our experiment, or possibly that the CR-39 data could be uncorrected for geometric acceptances that are significantly away from 1.0.

For Pb targets, the average ratio is very much in line with those found for the C, Al, and Cu targets, 0.76, but with a much larger standard deviation, 0.23. As with the other targets, the agreement is best for the smallest charge changes and gets worse as ΔZ increases.

1. Comparison to Models – Large Acceptance

Straightforward models based on measured fragmentation cross sections, including factorization and scaling from hydrogen-target data, may prove adequate for particular accuracy requirements in particular domains. For example, Webber et al. have presented a highly-evolved calculational method for hydrogen targets in Ref. 10, and various groups have shown that particular data sets can be accurately represented by factorization models. However, such methods do not appear to be applicable to arbitrary combinations of beam ion, energy, and target material. As pointed out by Wellisch [31], models of hadronic interactions fall into three broad categories: data-driven, parameterization-driven, and theory-driven. The absence of large cross section databases for nucleus-nucleus collisions precludes a purely data-driven ap-

proach, and QCD cannot, for various reasons, directly address the problem, ruling out a purely theory-driven approach. Thus models of nucleus-nucleus collisions have therefore typically mixed the parameterization-driven and theory-driven approaches, with theories – the dual-parton model (DPM), various versions of quantum molecular dynamics (QMD), etc. – that are rooted in phenomenology and are not fundamental. As a result, the models inevitably contain some number of adjustable parameters that can be tuned to data. It seems likely that tuning with a very limited number of data points will produce a model that is accurate only in a similarly limited region of the beam ion/energy/target space. Further, as we have noted here and elsewhere, systematic differences between experiments can be significant, and they limit the precision of any such tuning. To the best of our knowledge, none of the models has undergone a comprehensive tuning process that uses all available fragmentation cross section data and accounts for the (sometimes underestimated) experimental errors.

The general trend of the data in Figure 10 is for the fractions to decrease with increasing ΔZ, over most of the range. It is therefore tempting to fit these data, especially for the hydrogen target, with functional forms (e.g., exponentials) that are monotonically decreasing functions of ΔZ. One might accommodate the odd-even effect with two separate fits, one for even-Z fragments and another for odd. However, two salient facts argue against such an approach. First, when the cross sections for fragments with charge well below half the beam charge are included (as they are here, but not typically), and when we look at targets other than H, the simple monotonic trend clearly does not hold. For carbon and higher-A targets, the cross sections for fragments with charges less than 9, are invariably larger than those for Z = 9 production, which apparently represents a minimum for all beams. (This may be due to the shell structure of F, in which the last proton is weakly bound.) Second, though not explicitly considered here, it is quite apparent from Figure 10 and Tables 4 to 6 that – excluding hydrogen targets – the cross sections for fragments with Z less than 5 represent a significant fraction of the total, one that increases with A_t. Thus if the data in Figure 10 were extended to larger ΔZ for those targets, it would certainly show even stronger upturns than it does. Any monotonically decreasing functional form that attempts to describe this behavior can therefore be considered as, at best, an approximation that holds over a limited part of the ΔZ spectrum, but one that will grossly underestimate the cross sections of the lightest fragment species.

In contrast to the other targets, the H-target data do indeed fall monotonically (modulo the odd-even effect) with increasing ΔZ, at least for the range covered in these experiments. The difference between H and other target materials at both small and large ΔZ suggests a fundamental difference in the physics of the interaction. As we have pointed out elsewhere [32], a proton cannot deposit energy in the heavy beam ion as effectively as a nucleus, for a given impact parameter and energy per nucleon. This very basic difference in the nature of the collision suggests that scaling from hydrogen-target data to higher A_t is inherently problematic.

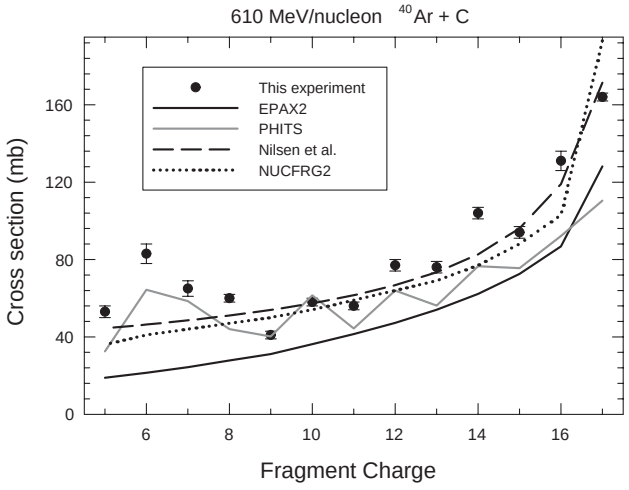

FIG. 15: Fragment cross sections for 610 MeV/nucleon ^{40}Ar beam on carbon compared to several models.

In Figure 15, we show the predictions of several models for 610 MeV/nucleon ^{40}Ar on carbon, along with the data. The models shown are EPAX2 [33], NUCFRG2, PHITS, and a model due to Nilsen et al. [34] based on heavier projectiles. We show the comparison for a single beam ion/energy/target combination, but the results are representative. The widest discrepancy is seen for EPAX2, which is below the data at every point and falls smoothly, in contrast to the even-Z enhancements in the data, particularly for charge 14. On average, the ratio of the predicted to measured cross section is 0.59. The Nilsen et al. parameterization also yields a smooth, monotonically-decreasing curve, but it is much closer to the data, with an average ratio of predicted to measured cross section of 0.92. The NUCFRG2 results are, for fragment charges 15 and below, quite close to (though systematically smaller than) the Nilsen model. The average ratio for NUCFRG2 is 0.86. Like the other models, PHITS predicts cross sections that are also generally below the data, with an average ratio of 0.83, but unlike the other models shown here, PHITS shows good agreement with the data for fragment charges 9 through 11, correctly predicts the upturn below charge 9 accompanied by the drop at charge 5, and clearly shows the odd-even effect in the 8 to 15 range. So, although the average agreement between PHITS and the data is comparable to that of the other models, these details suggest that the underlying physics is being better approximated in PHITS than in the other models. It should be noted that calculations with FLUKA [35] can also be expected to show the odd-even effect [36]. because it uses RQMD (similar to JQMD in PHITS).

2. Comparison to PHITS at Small Acceptance

In previous work [5], we showed comparisons of the charge spectra predicted by PHITS to measured spectra using a carbon beam at 400 MeV/nucleon, as seen at large acceptance (7.3°) and small acceptance (2.5°). The version of PHITS used for that work was 1.70; the present work uses version 2.13. In [5], we found that PHITS was fairly close to the data over most of the large-acceptance spectrum, but was far off from the data at small acceptance. The disagreements seen there are consistent with the hypothesis that the PHITS simulation produces fragment angular distributions that are considerably broader than in the data. Here, with much heavier beams, and an updated simulation code, similar comparisons yield very different conclusion. As a check on the difference in versions of PHITS, we re-ran simulations of a few of the ^{12}C data sets, and we find that the trend seen using the earlier version is still present in the newer version.

To get a quantitative handle on the angular distributions produced by PHITS, a straightforward test was performed to compare the acceptance as a function of fragment charge predicted by PHITS to that predicted by a simple Monte Carlo model that incorporates Tripathi and Townsend's modification [37] of the Goldhaber formulation [3]. In the simple model, the nuclear contribution to the angular distribution is added in quadrature to that from Coulomb multiple scattering; in the example chosen, 650 MeV/nucleon ^{40}Ar on a 4 g cm^{-2} carbon target, the latter is negligible. To compute the acceptance in PHITS, events were generated as described above, with detector volumes treated as voids. PAW ntuples were created for each acceptance, and the "event record" ntuples included an entry for the charge of the highest-charge particle (Z_{max}) crossing the volume in each event. The ntuples were used to create histograms of Z_{max} at both large (7.3°) and small (1.87°) acceptances, and then the latter histogram was divided by the former to obtain the acceptance as a function of fragment charge.

The acceptance results for PHITS are shown as a gray line in Figure 16, and those for the simple model are shown as a dashed black line. For the simple model, 10^5 fragments are generated per isotope. For most species, a single isotope (the most abundant naturally occurring) is used, with exceptions made for B (masses 10 and 11 are simulated), Be (7 and 9), Li (6 and 7), He (3 and 4), and H (1 and 2). The initial fragment trajectories were calculated starting at the (randomly thrown following an exponential distribution) point of interaction in the target and followed, allowing for Coulomb scattering in the remainder of the target and intervening detectors, to the small-acceptance detectors. The numbers of fragments with a given Z and A that remain within the various acceptances are scored and normalized to the number generated. The nuclear contribution depends on the σ_0 parameter in the Goldhaber model. A value of 120 MeV/c was found [5] to describe ^{12}C beam data at 290 and 400 MeV/nucleon. Here, we find that using a value of 110 MeV/c in the simple model gives a good match to PHITS.

As Figure 16 clearly shows, the agreement between PHITS and the simple model is very good for fragment charges from 6 to 17. (It is better than 2% for charges 9 to 18.) The ratio of the acceptance in the simple model to that in PHITS, divided by ten for convenience, is also shown in Figure 16, along with a dotted line to indicate that perfect agreement would correspond to a straight line at 0.1. For charges 3 through 5, the acceptance in the simple model is higher than that predicted by PHITS by 5 to 10%. For charges 2 and especially 1, the acceptance in PHITS appears to be much larger than that in the simple model, but this is an artifact of the method. In the PHITS simulation, the full multiplicity of fragments is produced and tracked. Thus many events recorded as having a "leading" charge 1 or 2 fragment in the small-acceptance detector had a heavier leading fragment seen in the large-acceptance detector, and consequently the number of events with a charge 1 leading fragment are seen at small acceptance. This accounts for the "acceptance," which in this instance is something of a misnomer, being greater than 1.0 for H and approaching 1 for He. Given this effect, it is only reasonable to compare the two acceptance models for charges 3 and higher, and in that range, the agreement is found to be quite good. Thus, in contrast to the previously-reported ^{12}C beam results, PHITS produces reasonable fragment angular distributions for these heavier beam ions. It is possible that JQMD does not accurately reproduce these distributions with lighter beam ions because it ignores quantum effects such as shell closure, and/or because it (like any QMD model) is affected by single-particle fluctuations; these effects can be important for light ions, and might significantly affect the accuracy of the simulated radial density profiles.

VI. CONCLUSIONS

Charge-changing and fragment production cross sections for several beams in a narrow range of projectile mass, from 35 to 48, have been obtained and compared to other measurements and to several models. The comparisons with other data are limited to ^{40}Ar beams, and agreement is found to be generally good for both types of cross sections. In comparing to models, we have chosen to focus on the analytic code NUCFRG2, used in current NASA transport codes, and PHITS, a larger, more complex Monte Carlo code that incorporates several models to simulate nuclear interactions. Considering first charge-changing cross sections, for both models, the highest level of accuracy is found for the ^{35}Cl beams and all targets. For other beams, NUCFRG2 accurately predicts the hydrogen-target charge-changing cross sections (typically within the uncertainty on the measurement), but shows discrepancies that tend to increase as the target mass increases. Combining all beams, and all targets

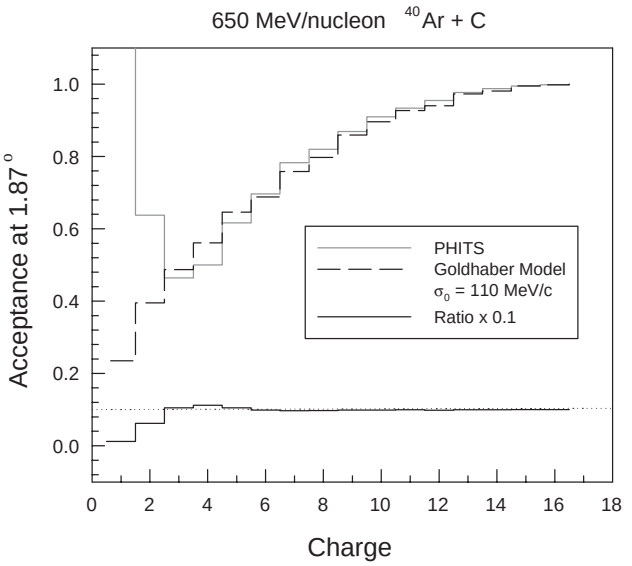

FIG. 16: Acceptance as a function of fragment charge at small angles for 650 MeV/nucleon ^{40}Ar beam on a 4 g cm^{-2} carbon target for a simple model and for PHITS.

heavier than H, NUCFRG2 cross sections are, on average, 5.6% below the data. PHITS, in contrast, shows a similar level of accuracy for targets heavier than H, but is much less accurate for H targets, being off by an average of 11.8% when using the default version of the Bertini model. However, when using JQMD for the H targets, the calculated cross sections are within 3% of the measurements for all beam ions and energies reported here. The level of agreement seen for these beams and targets is, in general, slightly worse than those reported in our previous experiments using other beams. Because fragmentation of heavy ions in the GCR in shielding materials will reduce dose in inhabited areas, systematic underestimates of charge-changing cross sections will lead to overestimates of dose and the amount of shielding required to achieve a particular level of dose reduction.

In comparing the fragment production data to models, it is readily apparent that older models in which the cross sections monotonically decrease with increasing charge change are inadequate, as illustrated in Figure 15. In contrast to the predicted smoothly-falling behavior, fragment cross sections in fact increase below charge 9, and show a significant odd-even effect across the range of fragment charges. The magnitude of the odd-even effect clearly depends on the z component of isospin (i.e., the neutron excess) of the projectile, and at least for $T_z = 0$ appears to depend on energy when hydrogen targets are considered. None of this complicated behavior is accurately predicted by simple models in which the cross sections simply fall as the fragment charge decreases. And while PHITS (using JQMD) does not, on average, predict fragment cross sections any more accurately than most other codes, it has two important features lacking in the other models considered here: first, it predicts the existence of the odd-even effect, and second, it predicts cross sections that rise (as the data do) in going from charge 9 to 8 to 7 to 6, and then fall for charge 5 (the lowest fragment charge measured here). This qualitative agreement with the data suggests that PHITS holds far more promise for further development than the older, simpler models and parameterizations.

Finally, we note that the evident differences between hydrogen-target fragment cross sections and those obtained with other targets (see Figure 9) suggest that the concept – applied by many modelers – that H-target data can be scaled to accurately predict cross sections with heavier targets is problematic. The differences between H and other targets are significant, particularly when light fragment production cross sections are considered. It seems intuitively clear that hydrogen typically does not deposit enough energy in the projectile to disrupt it and produce light fragments, while heavier target nuclei do. Thus hydrogen target cross sections continue to fall as fragment charge decreases, in contrast to all other target materials. It would seem, based on Figure 9 and similar figures we have shown in articles describing other data, that a more suitable starting point for a scaling model could be (comparatively sparse) carbon-target data. Scaling from H-target data may be successful if the energy is re-scaled as is done in the cross section model [38] used in the one-dimensional deterministic particle and heavy ion transport code HIBRAC [39, 40].

Acknowledgments

We gratefully acknowledge the efforts of the HIMAC accelerator operators, in particular Dr. Eiichi Takada, for providing us with excellent beams and stable conditions in this and other experiments. As well, two of us (J.M. and L.H.) thank the Japanese Society for the Promotion of Science for travel funds in support of this effort. We thank the operators of the NASA Space Radiation Laboratory at the Brookhaven National Laboratory for their efforts to provide the chlorine and titanium beams. We also acknowledge the great work done by Drs. Rusek, Chang, and Sivertz at the NSRL, who between them have created an extremely efficient and collegial environment. This work was supported at LBNL by the Space Radiation Health Program of the National Aeronautics and Space Administration under NASA Grant Numbers L14230C and H31909D, through the U.S. Department of Energy under Contract No. DE-AC03076SF00098. At HIMAC, this work was supported in part by the Research Project with Heavy Ions at NIRS-HIMAC, Project No. P037.

[1] *NCRP Report No. 98* (National Council on Radiation Protection and Measurements, 1989), p. 22.

[2] J. W. Wilson, F. A. Cucinotta, M.-H. Y. Kim, and W. Schimmerling, Physica Medica **XVII, Supp. 1**, 1 (2001).

[3] A. Goldhaber, Phys. Lett. B **53**, 306 (1974).

[4] C. Zeitlin, A. Fukumura, L. Heilbronn, S. Guetersloh, Y. Iwata, J. Miller, and T. Murakami, Nucl. Phys. A p. 341 (2007).

[5] C. Zeitlin, S. Guetersloh, L. Heilbronn, J. Miller, A. Fukumura, Y. Iwata, and T. Murakami, Physical Review C (Nuclear Physics) **76**, 014911 (pages 21) (2007), URL `http://link.aps.org/abstract/PRC/v76/e014911`.

[6] W. Webber, J. Kish, and D. Schrier, Phys. Rev. C **14-2**, 520 (1990).

[7] C. Knott, S. Albergo, Z. Caccia, C.-X. Chen, S. Costa, H. Crawford, M. Cronqvist, J. Engelage, P. Ferrando, R. Fonte, et al., Phys. Rev. C **53**, 347 (1996).

[8] G. Iancu, F. Flesch, and W. Heinrich, Radiat. Meas. **39**, 525 (2005).

[9] C.-X. Chen, S. Albergo, Z. Caccia, S. Costa, H. J. Crawford, M. Cronqvist, J. Engelage, L. Greiner, T. G. Guzik, A. Insolia, et al., Phys. Rev. C **56**, 1536 (1997).

[10] W. Webber, A. Soutoul, J. C. Kish, and J. M. Rockstroh, Astrophysical Journal Supplement **144**, 153 (2003).

[11] C. Zeitlin, K. Frankel, W. Gong, L. Heilbronn, E. Lampo, R. Leres, J. Miller, and W. Schimmerling, Rad. Meas. **23**, 65 (1994).

[12] C. Zeitlin, J. Miller, L. Heilbronn, K. Frankel, W. Gong, and W. Schimmerling, Rad. Res **154**, 655 (1996).

[13] C. Zeitlin, L. Heilbronn, J. Miller, S. E. Rademacher, T. Borak, T. R. Carter, K. A. Frankel, W. Schimmerling, and C. E. Stronach, Phys. Rev. C **56**, 388 (1997).

[14] C. Zeitlin, A. Fukumura, L. Heilbronn, Y. Iwata, J. Miller, and T. Murakami, Phys. Rev. C **64**, 024902 (2001).

[15] C. L. Tessa, S. Guetersloh, L. Heilbronn, J. Miller, L. Sihver, and C. Zeitlin, Adv. Space Res. **35**, 223 (2005).

[16] J. W. Wilson, L. W. Townsend, W. Schimmerling, G. K. Khandelwal, F. Khan, J. E. Nealy, F. A. Cucinotta, L. C. Simonsen, J. L. Shinn, and J. W. Norbury, NASA Reference Publication 1257 (1991).

[17] H. C. Bradt and B. Peters, Phys. Rev. **77**, 54 (1950).

[18] J. W. Wilson, J. L. Shinn, L. W. Townsend, R. K. Tripathi, F. F. Badavi, and S. Y. Chun, Nucl. Instrum. Methods Phys. Res. B **94**, 95 (1994).

[19] H. Iwase, K. Niita, and T. Nakamura, J. Nucl. Sci. Technol. **39**, 1142 (2002).

[20] R. Brun, O. Couet, C. E. Vandoni, and P. Zanarini, Comput. Phys. Commun. **57**, 432 (1989).

[21] C.-X. Chen, S. Albergo, Z. Caccia, S. Costa, H. J. Crawford, M. Cronqvist, J. Engelage, P. Ferrando, R. Fonte, L. Greiner, et al., Phys. Rev. C **49**, 3200 (1994).

[22] C. Zeitlin, L. Heilbronn, J. Miller, L. Townsend, and J. W. Wilson, Radiat. Res. **154**, 655 (1996).

[23] J. W. Wilson, private communication (2007).

[24] R. K. Tripathi, F. A. Cucinotta, and J. W. Wilson, Nucl. Instrum. Methods Phys. Res. B **117**, 347 (1996).

[25] K. Niita, S. Chiba, T. Maruyama, T. Maruyama, H. Takada, T. Fukahori, Y. Nakahara, and A. Iwamoto, Phys. Rev. C **52**, 2620 (1995).

[26] K. Niita, H. Takada, S. Meigo, and Y. Ikeda, Nucl. Instrum. Methods Phys. Res. B **184**, 406 (2001).

[27] J. Cugnon, Phys. Rev. C **22**, 1885 (1980).

[28] J. Cugnon, T. Mizutani, and J. Vandermeulen, Nuclear Physics A **352**, 505 (1981).

[29] S. Furihata, Nucl. Instrum. Methods Phys. Res. B **171**, 251 (2000).

[30] C. Zeitlin, S. B. Guetersloh, L. Heilbronn, and J. Miller, Nucl. Instrum. Methods Phys. Res. B **252**, 308 (2006).

[31] J. P. Wellisch, Nucl. Instrum. Methods Phys. Res. A **502**, 669 (2003).

[32] C. Zeitlin, L. Sihver, C. L. Tessa, D. Mancusi, S. Guetersloh, L. Heilbronn, and J. Miller, Radiation Measurements (2007).

[33] K. Summerer and B. Blank, Phys. Rev. C **61**, 034607 (2000).

[34] B. S. Nilsen, C. J. Waddington, J. R. Cummings, T. L. Garrard, and J. Klarmann, Phys. Rev. C **52**, 3277 (1995).

[35] A. Fasso, A. Ferrari, J. Ranft, and P. R. Sala, Tech. Rep. CERN-2005-10, CERN (2005).

[36] L. Pinsky, private communication (2007).

[37] R. K. Tripathi and L. W. Townsend, Phys. Rev. C **49**, 2237 (1994).

[38] L. Sihver, C. H. Tsao, R. Silberberg, T. Kanai, and A. F. Barghouty, Phys. Rev. C **47**, 1225 (1993).

[39] L. Sihver, D. Schardt, and T. Kanai, Jpn. J. Med. Phys. **18**, 1 (1998).

[40] L. Sihver and D. Mancusi (2007), in press.